Chapter 4

HIGH-EFFICIENCY ELECTRO-OPTIC METASURFACES USING BARIUM TITANATE

The material in this chapter was in part presented in [96, 135].

Rapid advances in information technology necessitate the development of functional devices that can meet the growing demands of modern data processing and communication systems. These devices must operate at ultrafast speeds, consume minimal power, and integrate seamlessly into compact architectures to keep pace with increasing data complexity and volume. Beyond conventional electronics, photonic platforms hold the promise to address these requirements, providing several benefits including high-speed operation, low energy dissipation, and high accuracy [136–139]. Achieving these capabilities hinges on the exploration of functional optical materials that are tailored for next-generation optical processing units.

The development of low-power photonic devices relies on materials with strong electro-optic responses in thin-film form. Silicon on insulator (SOI) technology is a widely adopted material platform for silicon photonic circuits due to its compatibility with CMOS processes [140–142]. However, its optical tunability is limited, as refractive index changes are primarily driven by thermo-optic effects [5, 80] or material doping [143], which typically result in longer response times or higher losses. Transition metal dichalcogenide (TMDC) monolayers have emerged as promising alternatives, offering gate tunability, strong light-matter interactions, tunable bandgaps, and short response times [132, 144, 145]. Despite these advantages, TMDC-based devices often exhibit narrow operational bandwidths, limiting their versatility in broadband applications, and require large interaction lengths due to their atomically thin active medium.

This chapter focuses on the use of electro-optic materials, specifically barium titanate, to overcome these challenges and realize high-efficiency active metasurfaces with low power consumption. We begin with an overview of the theory for electro-optic tuning. We will then introduce a novel synthesis technique for producing barium titanate thin films through spalling bulk single crystal substrates, followed by an experimental characterization of the physical and electro-optic thin film properties. As a first step toward realizing barium titante-based active metasurfaces,

we include simulations of high-efficiency transmissive structures for beam steering at visible frequencies. This chapter concludes with an outlook on future device architectures incorporating barium titanate for enhanced functionality.

4.1 Electro-optic tuning based on Pockels effect

The optical properties of an anisotropic medium can be described by the index ellipsoid, which takes its simplest form in the principal coordinate system as

$$\frac{x^2}{n_x^2} + \frac{y^2}{n_y^2} + \frac{z^2}{n_z^2} = 1. \tag{4.1}$$

In this equation, x, y, and z represent the principal axes, along which the displacement field $\mathbf{D}$ and the electric field $\mathbf{E}$ are parallel. The terms n_i correspond to the refractive indices in direction i, and the values $1/n_i^2$ represent the principal values of the optical impermeability tensor $\boldsymbol{\eta} = \epsilon_0 \boldsymbol{\varepsilon}^{-1}$, where ϵ_0 is the vacuum permittivity and $\boldsymbol{\varepsilon}$ the dielectric permittivity tensor. In certain crystals, applying an electric field alters both the size and orientation of the index ellipsoid. These changes are caused by shifts in the distribution of bond charges within the crystal and, in some cases, small deformations of the ion lattice [146], leading to a change in the impermeability tensor. The resulting modification in the refractive index ellipsoid is characterized through the electro-optic coefficients r_{ijk} and s_{ikl}, and is expressed as

$$\eta_{ij}(\mathbf{E}) - \eta_{ij}(0) = \Delta\eta_{ij} = r_{ijk}E_k + s_{ijkl}E_kE_l. \tag{4.2}$$

Here, r_{ijk} and s_{ijkl} represent the linear (Pockels) and quadratic (Kerr) electro-optic coefficients, respectively, both of which are material-dependent.

The Pockels effect occurs exclusively in non-centrosymmetric materials, which lack inversion symmetry. Among the 32 crystal point groups, 21 exhibit this property and can therefore display the Pockels electro-optic effect. These 21 groups are also piezoelectric. In contrast, the Kerr effect, a higher-order phenomenon, can occur in materials with any symmetry but it is typically much weaker. When the Pockels effect is present, the Kerr effect is generally negligible. The following discussion will focus on the Pockels effect and its application in active metasurfaces.

Given the symmetry of the dielectric permittivity tensor, the impermeability tensor is also symmetric. As a result, the indices i and j in equation (4.2) can be permuted, such that $r_{ijk} = r_{jik}$. This symmetry reduces the number of independent Pockels

coefficients from 27 to 18 and allows the use of a contracted notation for the electro-optic tensor [146] where

$$\begin{aligned} r_{1k} &= r_{11k} \\ r_{2k} &= r_{22k} \\ r_{3k} &= r_{33k} \\ r_{4k} &= r_{23k} = r_{32k} \\ r_{5k} &= r_{13k} = r_{31k} \\ r_{6k} &= r_{12k} = r_{21k}. \end{aligned} \tag{4.3}$$

Under an applied electric field, the deformed index ellipsoid can then be written as

$$\begin{aligned} &\left(\frac{1}{n_x^2}+r_{1k}E_k\right)x^2 + \left(\frac{1}{n_y^2}+r_{2k}E_k\right)y^2 + \left(\frac{1}{n_z^2}+r_{3k}E_k\right)z^2 \\ &\quad + 2yzr_{4k}E_k + 2xzr_{5k}E_k + 2xyr_{6k}E_k = 1. \end{aligned} \tag{4.4}$$

Here, E_k represents a component of the applied electric field with $k = 1, 2, 3$ (corresponding to x, y, z). Generally, the principal axes of the deformed ellipsoid do not coincide with the unperturbed axes, x, y, z, and must be determined through a principal axis transformation, through which one can extract the refractive index modulation.

The index modulation achieved through the electro-optic Pockels effect in dielectric materials is particularly advantageous for realizing low-loss metasurfaces capable of supporting ultra-fast modulation frequencies exceeding 100 GHz, as demonstrated in electro-optic modulators [147]. This makes them highly suitable for applications requiring spatiotemporal modulation of light, which was motivated in the previous chapter.

Lithium niobate ($LiNbO_3$, LN), long regarded as the benchmark for bulk electro-optic telecommunication applications, has recently attracted renewed attention in its thin-film form. Thin film LN enables enhanced performance in nanophotonic devices through an increased integration density [148–150]. It exhibits a Pockels coefficient of $r_{33} = 30.8$ pm/V, leading to an index change of 0.0022 under an applied field strength of 0.15 MV/cm [151]. However, the relatively small index change necessitates the design of high quality factor resonators (Q > 10,000) to achieve

significant modulation of scattered light [152]. Additionally, many existing active modulator designs require large applied voltages (> 20 V), which are incompatible with standard CMOS backplane architectures. Table 4.1 summarizes the electro-optic refractive index changes achieved in various nanophotonic devices using thin film electro-optic materials. For completeness, we also include a comparison to multiple quantum wells based on the quantum confined Stark effect. In these structures, a refractive index change occurs as a result of a shift in the interband transition energy when biased with an electric field [153–155]. Along with the experimentally observed index changes, Table 4.1 also highlights the wavelength coverage of these electro-optic materials, indicating their transparency window and thus suitability for high-efficiency nanophotonic modulators and active metasurfaces across a broad spectrum.

Active electro-optic material	Electro-optic coefficient (pm/V)	Applied field strength (MV/cm)	Δn	Wavelength coverage
Aluminum nitride (AlN)	r_{13} = 0.67 [156]	1.8 [157]	0.0006	300 nm - 8 μm [158]
Lithium niobate (LN)	r_{33} = 30.8 [151]	0.15 [159]	0.0022	420 nm - 5.2 μm [160]
Organic electro-optic (OEO) chromophore JRD1	r_{33} = 359 [161, 162]	0.05 [163]	0.005	Above 1.2 μm[c] [164]
Barium titanate (BTO)	r_{42} = 923 [165]	0.002 [165]	(0.0634)[a]	375 nm [166] - 7 μm [167]
Multiple quantum wells (MQW)	N/A	0.1 [75]	$\sim$ 0.002[b] [168, 169]	915-960 nm [75], 1.41-1.44 μm [168], 1.53-1.57 μm [169]

Table 4.1: **Refractive index change Δn for experimentally reported values of electro-optic coefficients for various thin films.** [a] The observed effective refractive index change in the BTO film will differ from this value due to the specifics of the orientation of different ferroelectric domains. [b] We report the index change values in the spectral region where the extinction coefficient k is relatively small. [c] Additional studies are needed to identify the upper bound of the operating wavelength.

Barium titanate (BaTiO3, BTO) stands out as a versatile perovskite material with exceptional dielectric, ferroelectric, piezoelectric, and electro-optic properties [170–

173]. Between 5°C and 120°C, BTO adopts a non-centrosymmetric tetragonal phase ($a = b \neq c$-axis) with its central titanium (Ti) ion displaced along one of the principal axes. This structural configuration gives rise to spontaneous polarization and a pronounced electro-optic response. The Pockels coefficients of bulk BTO (r_{42} = 1300 ± 10 pm/V, r_{33} = 105 ± 10 pm/V, r_{13} = 10.2 ± 0.6 pm/V) [139] far exceed those of widely used LN. Like other electro-optic materials, BTO supports ultrafast modulation frequencies ranging up to several hundred GHz [174, 175]. It furthermore exhibits a broad transparency window, spanning from 0.4 – 7 μm, as well as high refractive index values [139, 167], which facilitate the design of efficient resonators and waveguides across visible and near-infrared wavelengths. These properties make BTO an ideal material for next-generation photonic and optoelectronic devices. However, photonic integration often requires transitioning from bulk crystals to thin films, which presents several challenges.

4.2 Barium titanate thin films

Materials grown in thin film form are often polycrystalline or amorphous, and therefore typically exhibit lower electro-optic coefficients and reduced refractive index modulation compared to their single-crystal counterparts. The extent of this reduction is highly dependent on the growth method. For instance, BTO thin films grown using metalorganic deposition techniques are often 3-4 times lower than those of bulk materials [96, 173]. Table 4.2 provides an overview of the r_{42} coefficient reported for BTO prepared using various growth techniques. Currently, the highest quality BTO thin films have been achieved through molecular beam epitaxy with an electro-optic coefficient of r_{42} = 923 pm/V [165]. However, epitaxial growth process remains slow and expensive, limiting its scalability for large-area applications and it still does not match the electro-optic performance of bulk BTO.

To overcome the challenges associated with thin-film fabrication, we propose spalling to produce large-area, single-crystalline BTO thin films from bulk substrates. This low-cost, scalable technique has the potential to achieve large electro-optic coefficients, comparable to those obtained through epitaxial growth. Spalling is a recently developed kerfless method for separating layers from their host substrates, and was initially applied to III-V semiconductors [182]. In this process, a metal stressor layer is deposited on a bulk crystalline substrate, introducing compressive stress within the substrate. When the residual stress surpasses a critical

Synthesis method	Refractive index (λ = 1550 nm)	Electro-optic coefficient r_{42} (pm/V)	Modulation frequency
Bulk (top-seeded solution growth)	2.286 [176]	1300 [139]	< 0.1 GHz [177]
MBE [165]	2.286	923	65 GHz
PLD [178]	2.27	390	70 GHz
RF sputtering [179]	2.278	89	419 kHz
CVD [180]	2.13	4.5	17.3 kHz
CSD (sol-gel) [181]	(1.94 at λ = 633 nm)	(r_{eff} = 27 pm/V)*	5 MHz

Table 4.2: **Refractive index and electro-optic coefficient r_{42} for BTO synthesized using various techniques.** The reported refractive index values represent the average of the ordinary and extraordinary indices. The electro-optic coefficients correspond to measurements performed at the modulation frequencies specified in the adjacent column. *For sol-gel BTO, an effective electro-optic coefficient is reported due to the polycrystalline nature of the material.

threshold, a crack can be initiated with an external pulling force, such as exfoliation with tape.

There are two common approaches for creating spalled films. The first involves electroplating a tensile-stressed metal layer, such as nickel (Ni), to generate the stress required for crack propagation. The second relies on crystallization-induced stress in amorphous Si thin films deposited directly on the bulk substrate [183]. During annealing, the Si film undergoes crystallization and shrinkage, and thus generates sufficient stress for crack initiation. In this work, we adopt the first method, which utilizes electroplated Ni to create single-crystalline BTO thin films with controlled thickness and retained material properties.

Spalling single-crystal barium titanate

Figure 4.1a illustrates a schematic of our approach, which begins with the deposition of a 30 nm Ti and 30 nm gold (Au) seed layer on a single-crystal BTO substrate. This seed layer provides a strongly adhesive, conductive base for electroplating, as BTO itself is an insulating material. We then use a heated nickel chloride solution to electroplate 1-4 μm of Ni. The Ni thickness is primarily controlled by varying the plating time, while the solution temperature, plating current, and area are kept constant. The thickness of the spalled film, also referred to as the spall depth t, is determined by a force balance between the tensile force in the electroplated Ni, the

resulting compressive force in the BTO substrate, and the opening mode fracture along the crack introduced through the external pull force [182, 184]. In our setup, this external pull force is applied using a tape attached to a roller, which enables the exfoliation of continuous, single-crystalline BTO thin films. The resulting BTO spall is single-crystalline in nature, as confirmed through x-ray diffraction (XRD) scans shown in Appendix C.1.

The lateral dimensions of spalled BTO films currently range up to a few millimeters, as dictated by the 4.5 mm diameter of the plating aperture. However, prior studies on III-V semiconductors have demonstrated that spalling can be scaled to produce wafer-sized thin films [185, 186]. Additionally, bulk single-crystal BTO substrates can be reused for multiple spalling cycles by introducing repolishing techniques such as vibration polishing or chemical-mechanical polishing between cycles (see Appendix C.2). This reusability further enhances the cost-effectiveness of the proposed approach compared to alternative growth methods.

Figure 4.1b shows a spalled *c*-axis oriented (001), single-crystalline BTO thin film obtained through this procedure. The spalled BTO film rests on top of the Ti/Au seed layer, followed by the Ni layer and Kapton tape (from top to bottom). Optical microscopy reveals a large, continuous BTO area with lateral dimensions of approximately 1.5×3 mm^2, alongside smaller spalled regions. Discontinuities in the spalled film are attributed to nonuniform Ni plating and inconsistencies in the manual pull force. While Kapton tape was used in this demonstration, alternative tapes, such as polyvinyl alcohol (PVA) or heat-release tape, could enable easier transfer of spalled films to other substrates and will be explored in the subsequent discussion. A profilometer scan of the spalled substrate (Fig. 4.1c) along the dotted black line in Fig. 4.1b measures the spall depth, which ranges from 15 μm (middle inset) to less than 1 μm (right inset). The insets in Fig. 4.1c highlight surface corrugations, which vary from hundreds of nanometers in thicker regions (left inset) to tens of nanometers in thinner films (right inset). Areas with film thicknesses around 1 μm or less exhibit bright color variations under white light, indicative of thin-film interference effects. These observations are consistent across both (001) and (100) films spalled from single-crystal bulk substrates, as shown in Fig. 4.1d.

Thin film characterization

The brightly colored thin-film regions shown in Fig. 4.1, often obtained at the edges of spalled films, highlight the potential for producing larger-area films with

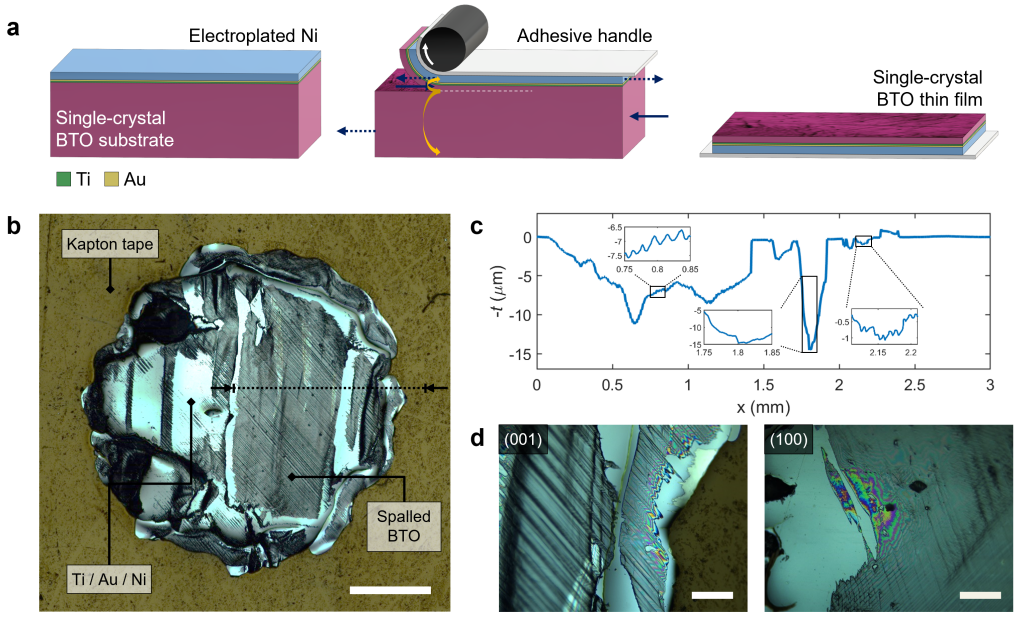

Figure 4.1: **Spalled barium titanate thin films.** (a) Schematic representation of procedure for spalling BTO. Left: A seed layer of Ti (green) and Au (yellow) is deposited on a bulk single-crystal BTO substrate. Ni (blue) is electroplated on top of the seed layer to induce compressive stress in the substrate. Middle: An adhesive handle (light grey) is stuck onto the substrate and can be peeled off with a roller (black). A force balance between the tensile (dotted, black) and compressive forces (solid, black) as well as the bending moment (orange) dictates the spall depth (white dashed). Right: The spalled single-crystalline BTO thin film is attached to the metal back layer and an adhesive handle. (b) Optical microscope image of spalled (001)-oriented BTO film. Scale bar: 1 mm. (c) Profilometer scan along black dotted line in (b), performed on the spalled substrate. The vertical axis indicates the negative of the spall depth $-t$, with zero corresponding to the level of the unspalled substrate. Insets show magnified height profiles corresponding to the square boxes, highlighting variations in spall depth and surface roughness. (d) Optical microscope images with spalled regions indicating thin film interference effects for (001)- and (100)-oriented films on the left and right, respectively. Scale bars: 100 μm.

sub-micron thicknesses that are suitable for photonic device integration. Achieving such films requires precise control over both thickness and surface roughness, which can be manipulated by adjusting the electroplated Ni thickness and thus the corresponding compressive stress induced in the bulk substrate. To further explore this for single-crystalline BTO, we electroplated two partially overlapping Ni layers onto a *c*-axis oriented single-crystal bulk BTO substrate, creating three distinct thickness regions, as shown in the inset of Fig. 4.2a. The first layer consisted of approximately 1.35 μm of Ni, followed by a partially offset second layer of 1 μm thickness. This configuration allowed us to spall BTO simultaneously from three regions, each subjected to a different stress state (from left to right: intermediate, high, and low). Performing all spalls simultaneously minimized variations caused by inconsistencies in the manual pull force.

Figure 4.2a shows an optical microscope image of the spall performed using PVA tape. The highest stress state (central area, blue box) yielded the largest spalled area, spanning millimeter-scale lateral dimensions and spall depths ranging from $5-7$ μm. The intermediate (orange box) and low-stress states (green box) yielded continuous BTO areas extending several hundred micrometers, with film thicknesses between $0.4-2.5$ μm and $0.1-1.8$ μm, respectively. Notably, the lowest stress state resulted in the thinnest and smoothest films, characterized by brightly colored areas exceeding 100×100 μm^2 and minimal surface features (Fig. 4.2b). To quantify surface roughness across different film thicknesses, we use atomic force microscopy (AFM). The scans shown in Fig. 4.2c correspond to the stress regime outlined in Fig. 4.2b (blue, orange, and green boxes) and reveal a decreasing root mean square (RMS) roughness r with decreasing thickness. Specifically, r corresponds to 125 nm in the high-stress region, 66 nm in the intermediate-stress region, and 27 nm in the low-stress region. RMS roughness was evaluated over the areas marked by white dashed boxes in Fig. 4.2c.

A similar analysis was performed for spalls obtained from (100)-oriented bulk crystals and is shown in Fig. 4.2d-f. For the spall shown in Fig. 4.2d, the three stress states were created by first electroplating approximately 2 μm of Ni, followed by a second layer with a thickness of $600-800$ nm. Due to the small difference in the Ni stressor layer thickness between the intermediate and high-stress regimes, only minimal differences in roughness are observed in the spalled films from these two regions. The spall depth t, measured via profilometry, ranges around $6-11$ μm

in most regions of the intermediate stress regime, while values between $t = 10 - 12$ μm are obtained for the high-stress regime.

Notably, finer features on the spalled films, such as horizontally or vertically oriented domain lines, extend across both the intermediate and high-stress regions, as seen in the blue box in image 4.2e. These features correspond to those found on the bulk substrate used for spalling, suggesting that the surface quality and domain structure of the bulk substrates are critical factors influencing spalled thin films (see Appendix C.3 for further discussion). While the surface quality is comparable between most parts of the high and intermediate-stress spalls, the second panel (orange box) in Fig. 4.2e reveals that small regions exhibiting thin-film interference can also be observed in the (100)-oriented films under intermediate stress conditions.

These thin film interference regions can be achieved more controllably by electroplating a thinner Ni layer, as shown in the low-stress regime. Because the Ni stressor thickness used in this case was smaller than that used for the (001)-oriented substrate, we obtain smaller spalled areas in this case. Nevertheless, we can identify thin film areas spanning up to tens of microns laterally, identified through the thin-film interference effect, as shown in the optical microscope image (green box, Fig. 4.2e). Due to the inherently lower surface quality of the (100)-oriented bulk BTO substrate, we observe some film breakage within the thin-film regions.

Figure 4.2f provides AFM scans of three different regions within the corresponding panels in Fig. 4.2e. The RMS roughness was evaluated over the white dashed regions in Fig. 4.2f and corresponds to approximately 235 nm in the high-stress state (top), 56 nm in the intermediate-stress regime (middle), and 47 nm for the low-stress regime (bottom).

AFM scans across a range of spalled film thicknesses allowed us to establish a relationship between roughness r and thickness t (Fig. 4.3a). Films spalled from both (001)- and (100)-oriented single-crystal substrates followed similar trends, with roughness approximating a square root function $r(t) \approx C \cdot t^{0.5}$, where C is a constant prefactor. For the fits shown in Fig. 4.3a, $C = 55.8$ and $C = 74.1$ for films obtained from (001) and (100) substrates, respectively, while the exponents are 0.45 and 0.40. Roughness was generally higher for (100)-orientated films, likely due to a more inhomogeneous domain structure in the bulk substrate, which contributed to greater initial surface roughness. Potential causes for this increased surface roughness in a-axis oriented substrates are discussed in Appendix C.3.

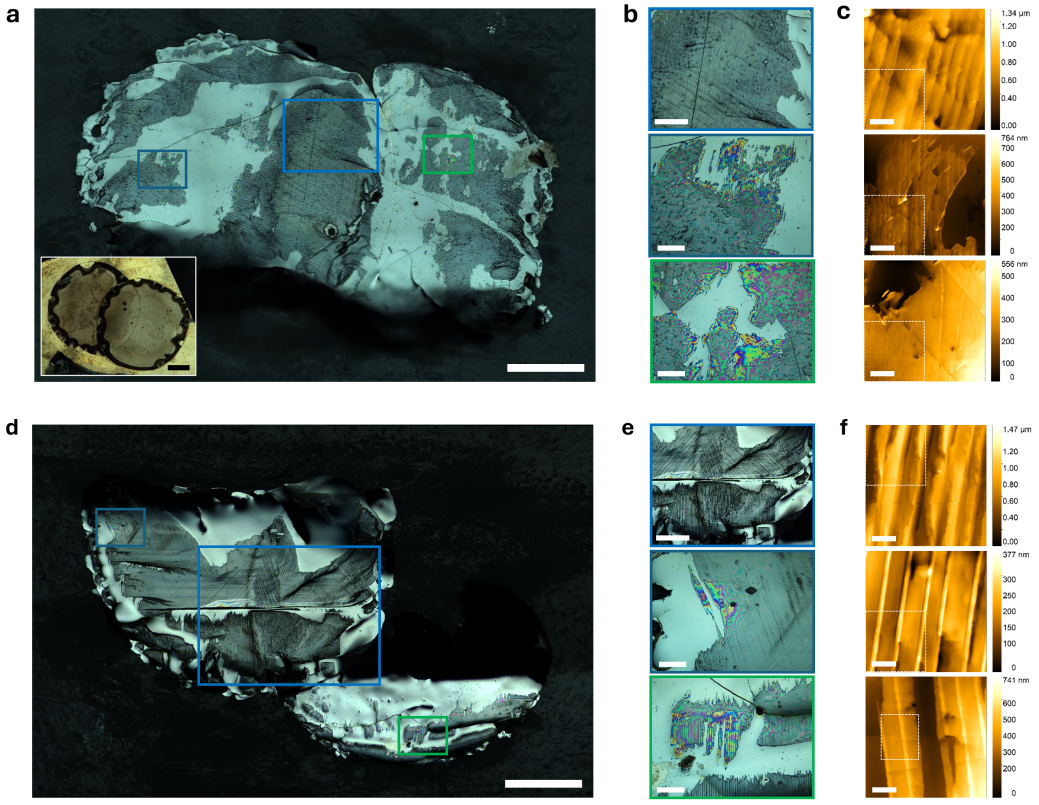

Figure 4.2: **Control over thickness of c- and a-axis spalled BTO films.** (a, d) Optical microscope image of (a) spalled (001) and (d) spalled (100) BTO thin film. The orange, blue, and green boxes indicate regions obtained through spalling with an intermediate, thick, and thin Ni stressor layer, respectively. Inset in (a) shows two overlaid circular electroplated Ni layers on top of a Ti/Au seed layer on the corresponding BTO substrate. Scale bars: 1 mm. (b, e) Optical microscope images of the area in the blue, orange, and green boxes in (a) and (d), respectively. (b) Scale bars (from top to bottom): 250 μm, 100 μm, 100 μm. (e) Scale bars (from top to bottom): 500 μm, 100 μm, 100 μm. (c, f) AFM images of (c) spalled (001) and (f) spalled (100) thin films within the areas shown in (b) and (e), respectively. The dashed white area in each image corresponds to the region over which the RMS roughness was evaluated. Scale bars: 10 μm.

Previous studies have reported a linear correlation between the spall depth and Ni stressor thickness when the stressor is significantly thinner than the substrate [182, 187]. This relation is due to greater compressive strain energy that is introduced into the substrate with increasing stressor thicknesses [182, 188, 189]. In ferroelectric materials such as BTO, such compressive strain can induce domain switching [190, 191]. To investigate this phenomenon further, we employed electron back scatter diffraction (EBSD) to map the crystal orientation across a thin film spalled from a (100) bulk crystal (a-axis). Figure 4.3b shows the band contrast image of the scanned area, reflecting the film's topography, alongside a crystal orientation map of a $60 \times 60\ \mu m^2$ area. The crystal orientation map reveals a large single-domain area (approximately $40 \times 15\ \mu m^2$) with (100) orientation in the upper half of the scanned region. A comparison of the band contrast image and the crystal orientation map indicates that regions with differing domain orientations correspond to topographical features in the scanned area.

These observations, combined with prior studies, suggest a strong correlation between the Ni stressor thickness, film thickness, and roughness in spalled BTO thin films. However, further studies are necessary to map the depth profile of the strain field in the substrate and understand the relation between film thickness, roughness, and domain switching. If domain switching in spalled BTO thin films occurs as a result of spalling, understanding whether it is a static process that occurs during electroplating of the stressor layer, or a dynamic process occurring as strain energy is released during exfoliation is crucial. Such insights will enable better control over spalled film properties, leading to targeted improvements in surface roughness and domain uniformity.

We also note that the initial quality of the bulk substrate, particularly its domain configuration, plays a critical role in determining the final domain structure and surface roughness of the spalled film. Using high-quality, single-crystalline (ideally single-domain) bulk substrates is therefore essential for producing smooth, spalled thin films of ferroelectric materials.

Thin film transfer

To fabricate functional devices from spalled films, it is necessary to transfer the films from the tape used for exfoliation onto a hard substrate. To facilitate this process, we perform the spall using water-soluble PVA tape for easy removal. The spalled film, adhered to PVA tape, is initially secured on a glass substrate.

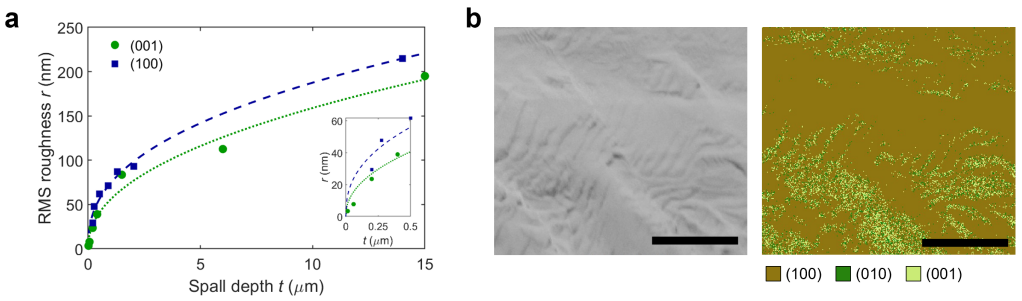

Figure 4.3: **Correlation of thickness and roughness in spalled BTO films.** (a) RMS roughness r of spalled (001) and (100) BTO films as function of the spall depth t. The inset highlights the roughness for spall depths below 500 nm. (b) Band contrast image (left) and corresponding crystal orientation map (right) obtained through electron backscatter diffraction. Scale bars: 20 μm.

Polypropylene carbonate (PPC) is then spin-coated over the entire sample to ensure uniform adhesion of the entire heterostructure to a polydimethylsiloxane (PDMS) stamp (Fig. 4.4a, d). The desired region is carefully cut out with a blade and picked up using the PDMS stamp, which is subsequently immersed in water to dissolve the PVA tape.

For substrate transfer, we use a resin that curable under ultraviolet (UV) light and semi-resistant to solvents. The PDMS stamp, now holding the spalled film, is positioned onto a drop of UV resin on the target substrate (Fig. 4.4b, e), with the Ni layer (Fig. 4.4b, blue) facing down. For this demonstration, we employ a silicon (Si) wafer with a 1 μm thick thermal oxide (silicon dioxide, SiO_2) layer. After curing the resin under UV light, the PDMS stamp is peeled off, and the sample is cleaned with acetone and isopropyl alcohol (IPA) to remove PPC residues on the spalled BTO film (Fig. 4.4c, f). Although some minor pitting is observed around the spalled area, likely due to the interaction between the solvent and the PPC residue adhering to UV resin, the spalled region itself remains clean and free from similar patterns. Importantly, the absence of gaps between the spall and the UV resin ensures that the surface roughness of the spalled remains unaffected during this process.

We use the transferred film shown in Fig. 4.4f to fabricate an electro-optically tunable device for characterizing the Pockels coefficient of spalled BTO thin films. In this device configuration, the electroplated Ni serves as both a metal back reflector and electrical contact. For applications requiring the removal of Ni, a two-step tape transfer process can be employed. In this approach, the spall is initially performed

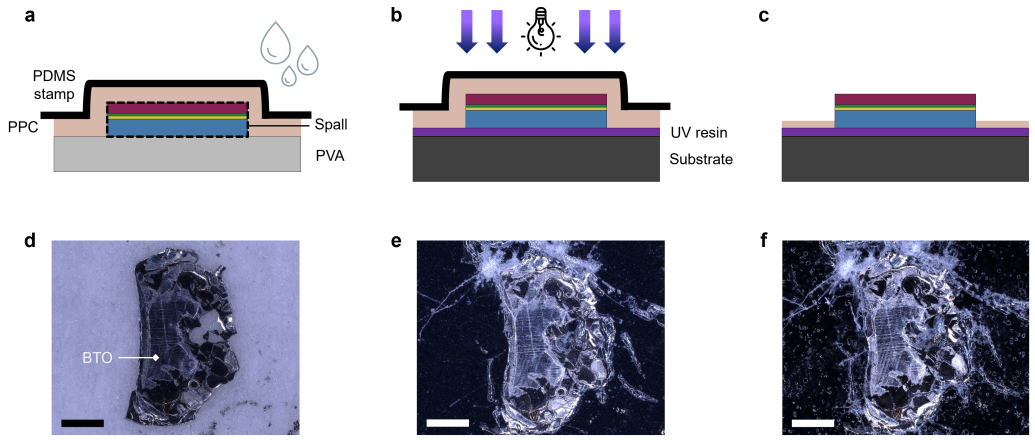

Figure 4.4: **Transfer of spalled film onto substrate.** (a) The spalled heterostructure (outlined by dashed black lines), consisting of Ni (blue), Au (yellow), Ti (green), and BTO (magenta), and adhered to PVA tape (gray), is spin-coated with PPC (tan) and picked up with a PDMS stamp (black). The PVA tape is then dissolved in water. (b) The spall is picked up with PPC/PDMS and adhered to a substrate (dark gray) with UV-curable resin (purple). The resin is cured under UV light (purple arrows). (c) After curing, the sample is cleaned with acetone/IPA to remove PPC from the spalled BTO. (d)-(f) Dark field optical microscope images of (d) spalled BTO film adhered to PVA and covered with PPC and PDMS, (e) spalled film adhered to PPC/PDMS on Si/SiO_2 wafer with UV resin, and (f) the transferred film after cleaning in acetone/IPA. Scale bars: 1 mm.

using a heat release tape, followed by a transfer to PVA tape with the BTO film facing downward. Once the spalled heterostructure is flipped, the procedure illustrated in Fig. 4.4 can be followed with the Ni layer exposed on top. The Ni layer can then be removed by immersing the stack in a Ni etchant, though this approach relies on the resistance of the UV-curable resin to the etchant.

For applications that require organic-free bonding, alternative methods such as wafer bonding may offer a viable solutions. However, applying heat and pressure to spalled BTO thin films could result in additional ferroelectric domain reorientation or even film breakage. Further research is needed to optimize bonding methods while preserving their structural and functional integrity.

4.3 Electro-optic characterization

To evaluate the functional properties of the spalled BTO thin films, we focus on characterizing their Pockels coefficient, a key parameter for electro-optic applica-

tions. As discussed in Section 4.1, noncentrosymmetric crystal groups, including BTO in its tetragonal phase, exhibit both electro-optic and piezoelectric effects. These effects are inherently coupled: The direct piezoelectric effect generates electric polarization in response to applied stress, while the converse piezoelectric effect induces strain under an applied electric field. This strain alters the refractive index through the photoelastic effect, which must be considered alongside the electro-optic effect to fully understand the material's behavior.

The Pockels tensor, which characterizes the electro-optic response, therefore includes contributions from three components: the piezoelectric, electronic, and ionic effects [192]. At low frequencies, from DC up to approximately 1 MHz, the photoelastic response dominates, as mechanical lattice deformations can follow the modulation signal. In this range, acoustic phonons also contribute to the modulation [193]. Above the acoustic phonon frequency, typically between 1 to 100 MHz, a crystal is considered to be 'clamped' because the mechanical deformations are too slow to respond to the modulation signal. At these frequencies, nonlinearities associated with optical phonons contribute to the Pockels effect and are referred to as ionic contributions. For frequencies exceeding the optical phonon range (around a few THz), these ionic contributions become negligible, and the electro-optic effect is primarily governed by electronic resonances, which have characteristic frequencies in the PHz regime.

To account for this frequency dependence, the Pockels tensor is typically divided into two parts: the unclamped tensor, which includes contributions from all three components and is observed up to few MHz, and the clamped tensor, which only reflects the higher frequency contributions [177]. Table 4.3 provides an overview of the unclamped and clamped electro-optic coefficients in bulk BTO.

Pockels coefficient	unclamped (pm/V)	clamped (pm/V)
$r_{13} = r_{23}$	10.2 ± 0.6	8 ± 2
r_{33}	105 ± 10	40.6 ± 2.5
$r_{42} = r_{51}$	1300 ± 100	730 ± 100

Table 4.3: **Pockels coefficients for bulk BTO in the unclamped and clamped case.** [139]

Given the frequency-dependent nature of electro-optic coefficients, it is crucial to characterize bulk BTO and spalled thin films across a range of modulation frequencies. Various techniques have been developed for this purpose, typically combining

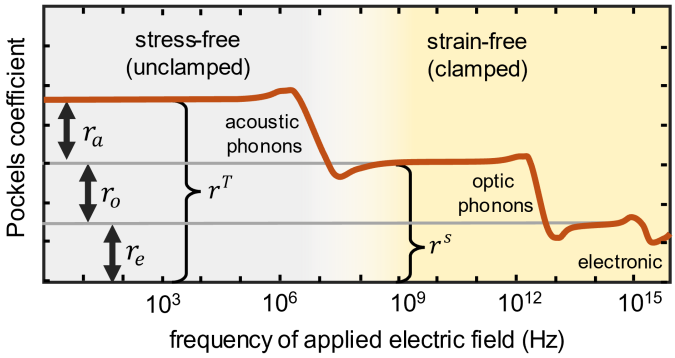

Figure 4.5: **Dispersion of electro-optic coefficient as function of modulation frequency.** Adapted from [194].

high-frequency electric fields with lock-in detection schemes for enhanced precision. These methods include interferometric approaches [195–197], transmission-based measurements [198, 199], as well as measurements leveraging integrated devices [200, 201]. Each approach offers unique advantages, such as increased sensitivity to small Pockels coefficients, the ability to resolve individual components of the Pockels tensor *vs* effective coefficients, and the varying levels of sample preparation [202].

In the following, we employ a Teng-Man reflectometry setup to characterize the Pockels coefficients of both bulk BTO substrates and spalled thin films. This method was selected for its high sensitivity and minimal sample preparation requirements, making it particularly well-suited for assessing electro-optic properties across different material forms. Below, we first outline the measurement procedure and subsequently present the experimental results for the characterization of bulk BTO and spalled thin films.

Teng-Man reflectometry

The Teng-Man measurement technique was originally developed for measuring the electro-optic coefficient r_{33} of poled polymer films [195, 196]. The experimental setup is shown in Fig. 4.6a, with the inset providing a schematic of the bulk BTO sample used for calibration. The incident laser beam is linearly polarized at 45°, ensuring equal amplitude for the *s*- and *p*-polarized components. Upon reflection from the sample, the beam propagates through a Soleil-Babinet compensator (SBC), an analyzer, and into a detector. The SBC functions as a continuously variable wave

plate, allowing precise control of the phase retardance through positional adjustment. A lock-in amplifier is used to modulate the sample.

The setup is used in two configurations: (1) with two irises before and after the sample, respectively, ensuring a probing diameter of less than 300 μm and signal collection from the reflected beam after a single pass through the sample (as shown in the inset of Fig. 4.6a), and (2) with two lenses in place of the irises to probe smaller areas with tens of microns diameter. In the first configuration, the reflected intensity is measured with the lock-in amplifier, while in the second, an oscilloscope can be used due to a stronger signal. For this study, configuration (1) is employed for measurements of the bulk sample, while both configurations (1) and (2) are used to evaluate spalled films for comparative analysis.

The working principle of Teng-Man reflectometry involves modulating the phase retardance between the s- and p-waves, denoted as Ψ_{sp}, using the SBC. The averaged output intensity is given by

$$I_{\mathrm{DC}} = I_0 + 2I_{\mathrm{c}} \cdot \sin^2\left(\frac{\Psi_{\mathrm{sp}} + \Psi_{\mathrm{c}}}{2}\right) = C_0 + C_1 \cdot \sin^2\left(\frac{\Psi_{\mathrm{sp}} + \Psi_{\mathrm{c}}}{2}\right). \tag{4.5}$$

Here, I_0 represents the background intensity, and I_{c} corresponds to half the maximum intensity. The compensator phase Ψ_{c} is controlled by adjusting the retardation setting and can be written as $\Psi_{\mathrm{c}} = C_2 \cdot x$, where x is the SBC position in millimeters. By fitting the DC intensity measurements at various SBC positions to equation (4.5), we can extract C_0, C_1, Ψ_{sp}, and C_2.

Next, a modulating voltage $V = V_m \cdot \sin(\omega_m t)$ at frequency $\omega_m = 2\pi f_m$ is applied across the sample. This induces a phase change $\delta\Psi$ in both the s- and p-waves due to changes in the refractive index, δn, and path length, δs, which are caused by the electro-optic effect. As a result, the phase change is given by $\delta\Psi = (2\pi/\lambda)(s\delta n + n\delta s)$, with λ corresponding to the optical wavelength. The modulated intensity, I_m, is obtained by differentiating I_{DC} by using a first-order approximation for V_m [203], and can be written as

$$I_m = \delta C_0 + \delta C_1 \cdot \sin^2\left(\frac{\Psi_{\mathrm{sp}} + \Psi_{\mathrm{c}}}{2}\right) + \frac{C_1}{2}\sin(\Psi_{\mathrm{sp}} + \Psi_{\mathrm{c}})\delta\Psi_{\mathrm{sp}}. \tag{4.6}$$

The second term corresponds to reflectivity changes due to refractive index variation, while the third term reflects contributions from the phase difference change $\delta\Psi_{\mathrm{sp}}$.

In the measurement, we record the absolute value of the modulated intensity $|I_m|$ at several positions and fit to equation (4.6) to obtain δC_0, δC_1, and $\delta\Psi_{\mathrm{sp}}$.

The Pockels coefficients are derived using $\delta\Psi_{\mathrm{sp}} = \Gamma_m \sin(\omega_m t)$, where Γ_m is expressed as

$$\Gamma_m = \left(\frac{2\pi r_{33} V_m}{\lambda}\right)\left[\frac{n_o n_e \sin^2\theta}{(n_e^2 - \sin^2\theta)^{1/2}} + \frac{r_{13}}{r_{33}}\left(\frac{n_o^3}{n_e}(n_e^2 - \sin^2\theta)^{1/2} - \frac{n_o^4}{(n_o^2 - \sin^2\theta)^{1/2}}\right)\right]. \tag{4.7}$$

Here, θ is the incident angle of light on the sample. When the output beam intensity is biased at the half-intensity I_c, the modulated intensity is in its most linear region. At this point, $I_m/I_c \approx \delta\Psi_{\mathrm{sp}}$. Substituting this relation into the equations above yields

$$r_{33} = \left(\frac{\lambda}{2\pi}\right)\left(\frac{I_m}{I_c V_m}\right)\left[\frac{n_o n_e \sin^2\theta}{(n_e^2 - \sin^2\theta)^{1/2}} + \zeta\left(\frac{n_o^3}{n_e}(n_e^2 - \sin^2\theta)^{1/2} - \frac{n_o^4}{(n_o^2 - \sin^2\theta)^{1/2}}\right)\right]^{-1}. \tag{4.8}$$

Here, we define $\zeta \equiv r_{13}/r_{33}$. For BTO, we assume $\zeta = 1/10$ based on the electro-optic coefficients reported in bulk BTO [139]. Under the approximation $n_o \approx n_e \approx n$, Eq. (4.8) simplifies to

$$r_{33} = \left(\frac{\lambda}{2\pi}\right)\left(\frac{I_m}{I_c V_m}\right) \cdot \frac{10(n^2 - \sin^2\theta)^{1/2}}{9n^2 \sin^2\theta}. \tag{4.9}$$

In our measurement, light is incident on the sample at $\theta = 45°$.

Bulk electro-optic characterization

To calibrate the Teng-Man setup and obtain reference values for the electro-optic coefficients of bulk BTO substrates used for spalling, we pattern (100)-oriented bulk substrates (a-axis) with top and bottom electrodes. The bottom electrode consists of a 5 nm Ti adhesion layer followed by a 100 nm Au layer and is contacted from the edge of the substrate using silver paste. For the top electrodes, we pattern three 50 nm thick ITO contacts, as shown in Fig. 4.6b. These top contacts are designed to enable probing of the electro-optic coefficients with both in-plane and out-of-plane electric fields. Each ITO top electrode also includes an Au bond pad (5 nm Ti / 80 nm Au) for electrical addressing. The choice of crystal orientation for bulk testing

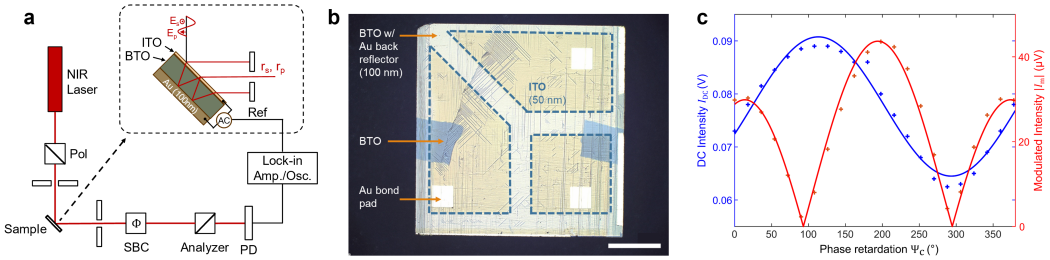

Figure 4.6: **Electro-optic measurement of bulk BTO.** (a) Schematic of Teng-Man measurement setup. The setup was verified using bulk BTO samples, consisting of a 100 nm thick Au back electrode and a 50 nm thick ITO top electrode (inset). Configuration (1) uses irises before and after the sample. In configuration (2), each iris is replaced with a lens with a focal length of $f = 3.5$ cm. Pol: Polarizer. PD: Photodetector. Lock-in Amp: Lock-in amplifier. Osc: Oscilloscope. Ref: Reference signal. (b) 0.5 mm thick (100)-oriented bulk BTO substrate with 100 nm thick Au back reflector and top electrodes consisting of 50 nm thick ITO (area inside gray dashed lines) and 1 mm^2 sized bond pads consisting of 5 nm Ti and 100 nm Au. Scale bar: 2.5 mm. (c) DC intensity I_{DC} (blue) and modulated intensity $|I_m|$ (red) obtained for bulk substrate shown in (b).

allows us to potentially probe both r_{33} and r_{42} coefficients, unlike (001)-oriented substrates (c-axis), which primarily facilitate r_{33} measurements.

Importantly, while the a-axis orientation allows measurement of additional electro-optic coefficients, it introduces in-plane birefringence. This birefringence causes the E_x and E_y components of the +45° linearly polarized incident plane wave to experience different refractive indices, resulting in a rotation of the polarization of the reflected beam. To account for this effect, the Teng-Man setup for a-axis samples requires the polarizer to be oriented at +45°, the SBC at +45° and the analyzer at approximately 0°. In contrast, c-axis films conventionally use a configuration with the polarizer, SBC and analyzer oriented at +45°, +90° and −45°, respectively. The measurement configurations are selected based on the expected shape of the I_{DC} and $|I_m|$ curves, with I_{DC} resulting in a single peak around a phase retardation of 180° and $|I_m|$ resulting in two maxima at the quadrature points of the DC curve. We refer to the first configuration as a-axis configuration while the second is referred to as c-axis configuration. All measurements on bulk substrates are performed at a wavelength of $\lambda = 1520$ nm.

In a first step, we probe the electro-optic coefficient on top of the ITO electrode area with an out-of-plane modulating field and the Teng-Man setup in the a-axis

configuration. Initial measurements yield an electro-optic coefficient of 4.1 pm/V. We then pole the bulk BTO substrate out-of-plane with a voltage of 200 V across a thickness of 0.5 mm (poling field of 4 kV/cm) for 1 hour. After poling, the Teng-Man setup is switched to the c-axis configuration to obtain clean measurements, yielding an electro-optic coefficient of 11.4 pm/V. We attribute this increase in the electro-optic coefficient to a reorientation of the domains from a-axis to c-axis in the probing region. However, due to a preferential (100) orientation of the substrate and a relatively small poling field, only partial reorientation occurs, resulting in an electro-optic coefficient smaller than the literature value for r_{33}.

To probe r_{33} more accurately with a (100)-oriented bulk substrate, we move the probing spot to an area between two ITO top electrodes in the bottom half of the substrate shown in Fig. 4.6b. This position allows application of an in-plane modulating field in a preferentially a-axis oriented region. We perform the measurements using an a-axis configuration of the Teng-Man setup and obtain an electro-optic coefficient of 22.3 pm/V. We then apply a voltage of 200 V between the two in-plane electrodes spaced 1 mm apart (poling field of 2 kV/cm), leading to a drastic increase in the measured electro-optic coefficient, which reaches 96.4 pm/V. This value is in good agreement with literature values for bulk BTO ($r_{33,\mathrm{lit}} = 105 \pm 10$ pm/V [139]). The corresponding measurements for I_{DC} and $|I_m|$ are shown in Fig. 4.6c, indicating clear peaks in the modulated intensity curve (red) at the quadrature points of the DC curve (blue).

Thin film electro-optic characterization

The Pockels coefficient of spalled BTO films is evaluated using the film shown in Fig. 4.4f. The spalled film, obtained from a c-axis bulk crystal, has a thickness of approximately 20 μm and lateral dimensions greater than 0.5×1.5 mm^2 (Fig. 4.7a). The Ni stressor layer beneath the BTO serves a dual purpose of a metal back contact and reflective surface. A transparent top electrode is patterned on top of the spalled BTO using shadow masks. This electrode consists of a 50 nm thick ITO layer (light green dashed region in Fig. 4.7a) that facilitates optical probing. The ITO layer is partially overlaid with a 5 nm Ti and 100 nm Au layer (brown dotted region in Fig. 4.7a) for wire bonding. This electrode configuration allows direct characterization of the r_{33} coefficient under an out-of-plane modulating field, given the c-axis orientation of the spalled BTO film.

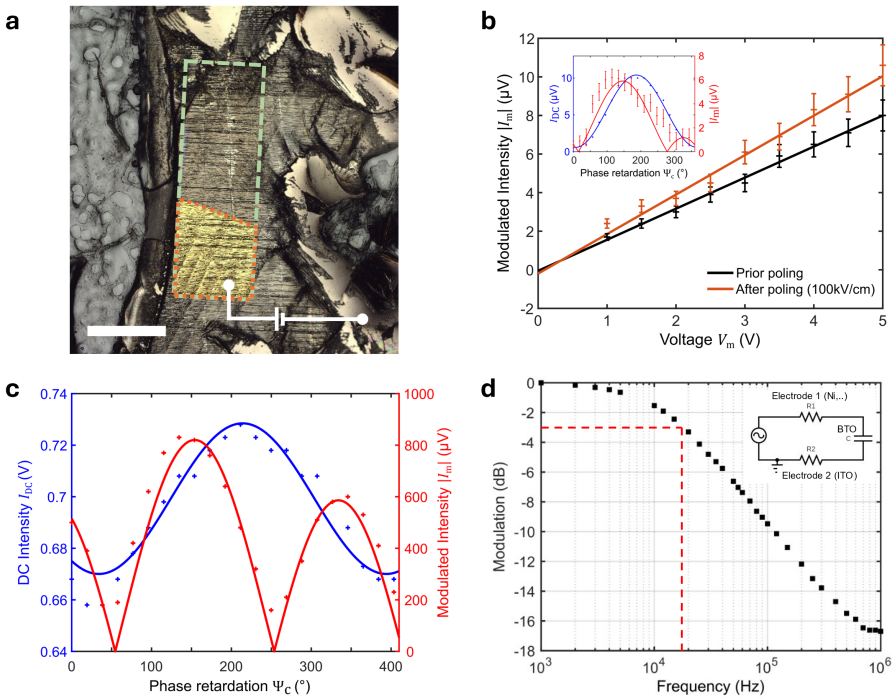

Figure 4.7: **Electro-optic measurement of spalled BTO thin film.** (a) Optical microscope image of BTO spall from Fig. 4.4f with ITO/Au top electrode. The light green dashed region indicates the area with transparent ITO for optical probing, the brown dotted region represents the area with Au on top of ITO. Wires are bonded to the Au top contact and Ni back layer, enabling probing of the electro-optic coefficients with an out-of-plane electric field. Scale bar: 500 μm. (b) Modulated intensity $|I_m|$ as a function of applied voltage V_m using configuration (1) of the Teng-Man setup. Inset: DC intensity I_{DC} (blue) and modulated intensity $|I_m|$ (red) as function of phase retardation Ψ_{c} for the sample shown in (a). Crosses represent measurement points, and the lines are the fits used to extract the Pockels coefficient. Error bars correspond to standard deviations and are deduced from repeated measurements. (c) DC intensity I_{DC} (blue) and modulated intensity $|I_m|$ (red) as function of phase retardation Ψ_{c} with configuration (2) of Teng-Man setup. (d) Normalized modulation intensity as a function of modulation frequency. The red dashed line indicates the -3 dB cutoff frequency at approximately 18 kHz. The inset illustrates the equivalent circuit of the device, with R1 and R2 representing the resistances of the top and bottom electrodes, and C representing the capacitance of the BTO layer.

We first perform measurements on the spalled film shown in Fig. 4.7a using configuration (1) of the Teng-Man setup with an iris before and after the sample. As outlined in the preceding sections, we begin by measuring the DC intensity as function of the phase retardation Ψ_c to calibrate the SBC, and then measure the modulated intensity curve. The inset of Fig. 4.7b shows a representative measurement for this case with I_{DC} plotted in blue and $|I_m|$ in red. As expected, I_{DC} reaches a minimum at $\Psi_c \approx 0°$ and 360° due to the cross-polarization of the polarizer and analyzer (Fig. 4.6a). Next, we apply a modulating voltage across the sample with V_m = 5 V at a frequency f_m = 10 kHz, which enables a measurement of the unclamped electro-optic coefficient [177, 193]. The modulated intensity $|I_m|$ is measured using a lock-in amplifier, with the red points in the inset of Fig. 4.7b representing averaged data over repeated measurements. Error bars denote standard deviations across these measurements. The values for I_{DC} and $|I_m|$ are then fitted to equations (4.5) and (4.6), respectively, and r_{33} is evaluated using equation (4.9) at the operating wavelength λ = 1500 nm. Using refractive index values for BTO from Ref. [173], we determine an electro-optic coefficient of r_{33} = 42 ± 3 pm/V. To confirm that the measured response is governed by the electro-optic Pockels effect, we demonstrate a linear relationship between the applied voltage V_m and the modulated intensity $|I_m|$ in Fig. 4.7b (black line), validating the fitted r_{33} value. The values for $|I_m|$ in Fig. 4.7b are recorded at $\Psi_c \approx 115°$, where the response is maximized.

We observe an asymmetry in the two peaks of the modulated intensity in the inset of Fig. 4.7b, which is attributed to surface roughness leading to scattering in the reflected signal, as well as partial polarization rotation due to domain switching during spalling. To limit the impact of these effects, we repeat the measurement after poling the spalled thin film with an out-of-plane field by applying a constant voltage of 20 V for one hour. This procedure increases the measured electro-optic coefficient to 55 ± 5 pm/V. Assuming the same ratio of r_{42}/r_{33} as in bulk BTO, we can project a value of r_{42} = 680 pm/V based on the measured r_{33} after poling. Although this value is lower than that of bulk BTO, it significantly exceeds those achieved using alternative bottom-up growth techniques such as sputtering or pulsed laser deposition (see Table 4.2).

Furthermore, based on the EBSD scans previously shown in Fig. 4.3b, we know that there is a correlation between domain orientation and surface roughness and that single-domain regions are tens of microns in size. To investigate the effect of

domain structure on the measured electro-optic coefficient, we perform a secondary measurement using configuration (2) of the Teng-Man setup, where the irises before and after the sample are replaced with lenses. With this change, we can reduce the optical probing diameter from several 100 μm to $\sim$ 50 μm and achieve a cleaner signal readout. As a result, the DC intensity and modulated intensity can be measured with an oscilloscope and are shown in Fig. 4.7c in blue and red, respectively. After fitting the data from a series of measurements, we obtain an electro-optic coefficient of r_{33} = 160 ± 40 pm/V, leading to a projected value of r_{42} = 1980 pm/V. Despite the nonideal roughness and domain structure of spalled BTO, these results suggest that bulk properties are preserved locally, particularly in potentially single-domain regions. We anticipate that future improvements to the electro-optic properties of spalled films will involve obtaining large-area thin films with low roughness or polishing thin films after spalling to get cleaner reflected signals. Moreover, poling thin films at elevated electric fields and temperatures may enable complete restructuring and stabilization of domains in the desired configuration.

All electro-optic measurements discussed until now were performed using a modulation frequency of 10 kHz. Figure 4.7d illustrates the frequency dependence of the modulated signal up to 1 MHz, showing a -3 dB cutoff frequency, $f_{-3\mathrm{dB}}$, at approximately 18 kHz. The decrease in modulation intensity is attributed to the RC time constant of the device, rather than a transition from unclamped to clamped Pockels coefficients. The circuit model for the spalled BTO film measured for electro-optic characterization is shown in the inset of Fig. 4.7d.

In the ideal case, $f_{-3\mathrm{dB}}$ can be approximated using the resistance of the ITO layer ($\rho_{\mathrm{ITO}} \approx 10^{-4}$ Ω·cm), the relative permittivity of BTO along the c-axis ($\varepsilon_{\mathrm{BTO,c}} \approx$ 135), the dimensions of the ITO top electrode (w_{ITO} = 0.5 mm, L_{ITO} = 1 mm), as well as the film thicknesses (t_{ITO} = 50 nm, t_{BTO} = 20 μm). However, the surface roughness of the spalled BTO film will introduce deviations from these values. Based on the results shown in Fig. 4.3a, we expect greater than 200 nm surface roughness for a 20 μm thick spalled BTO film. Since the ITO thickness is much smaller than the RMS roughness of the BTO film, current flow paths will be disrupted, increasing ITO resistivity as described by the Fuchs-Sondheimer model [204, 205]. Assuming an increase in ITO resistivity by two orders of magnitude ($\rho_{\mathrm{ITO,rough}} \approx 10^{-2}$ Ω·cm), the theoretical modulation bandwidth of the spalled film can be calculated as

$$f_{-3\mathrm{dB}} = \frac{1}{2\pi RC} = \frac{1}{2\pi} \times \frac{w_{\mathrm{ITO}} \cdot t_{\mathrm{ITO}}}{\rho_{\mathrm{ITO,rough}} \cdot L_{\mathrm{ITO}}} \times \frac{t_{\mathrm{BTO}}}{\epsilon_0 \cdot \varepsilon_{\mathrm{BTO,c}} \cdot L_{\mathrm{ITO}} \cdot w_{\mathrm{ITO}}} \approx 592\ \mathrm{kHz}. \tag{4.10}$$

Here, the conductivities of Ni and Au are neglected. R represents the resistance of the ITO electrode, C is the capacitance of the spalled BTO film, and ϵ_0 is the vacuum permittivity. Our calculations indicate that the upper limit of the frequency bandwidth for the current device is in the range of hundreds of kHz. Empirical data shows an even lower RC time constant for the measured device, which could be attributed to an even lower ITO resistivity and increased relative permittivity of BTO due to local variations in the domain structure. To accurately capture the transition from unclamped to clamped electro-optic coefficients, alternative device geometries will need to be explored.

Measurement procedure for characterization of r_{42}

Thus far, we have focused on an electro-optic characterization that relies on the same electrodes for both poling and probing, resulting in parallel poling and modulating fields. However, in the characterization of bulk BTO substrates, we noted that the in-plane birefringence of a-axis BTO substrates provides an opportunity to additionally probe the r_{42} coefficient with the Teng-Man setup.

To achieve this, an a-axis substrate or spalled film must first be poled using an in-plane field. Following this step, instead of applying a modulating field that is parallel to the poling field, electro-optic coefficients would be probed at an angle to the poling field. This requires patterning individual probing electrodes that are integrated within the gap between the poling electrodes. These electrodes can be oriented at various angles to the poling field to enable angle-dependent characterization of the electro-optic coefficients. With this configuration, it becomes possible to probe a linear combination of r_{33} and r_{42}. This approach is analogous to phase modulator designs utilizing an a-axis oriented BTO film with lateral electrodes positioned at approximately 45°, which maximize the effective electro-optic coefficient [204, 205].

Building on this understanding, we now shift the focus to design considerations aimed at maximizing the electro-optic index change. Specifically, we analyze the requirements for achieving high-performance active metasurfaces using BTO thin

films and explore designs for active transmissive metasurfaces optimized for operation at visible wavelengths.

4.4 Design strategy for maximal electro-optic index change

To maximize the electro-optic index change under an applied field, it is crucial to identify the optimal crystal orientation, the polarization of the electric field relative to the applied electric field $\boldsymbol{E}$, and the wavevector $\boldsymbol{k}$. The subsequent calculations assume a single-domain BTO thin film and use electro-optic coefficients reported for bulk barium titanate. Such properties can be realized over areas spanning tens of microns using the spalling procedure described above. For an analysis of the achievable index changes in the achievable index in multi-domain configurations of BTO thin films in comparison to single-domain regions, we refer the reader to Ref. [193].

As discussed in Section 4.1, the polarity of BTO in its tetragonal phase gives rise to a strong electro-optic response at room temperature and is defined by the following Pockels tensor

$$\mathbf{r} = \begin{pmatrix} 0 & 0 & r_{13} \\ 0 & 0 & r_{23} \\ 0 & 0 & r_{33} \\ 0 & r_{42} & 0 \\ r_{51} & 0 & 0 \\ 0 & 0 & 0 \end{pmatrix}. \tag{4.11}$$

In this tensor, the dominant electro-optic contributions arise from $r_{42} = r_{51} = 1300$ pm/V in bulk crystals [139]. Based on this tensor, the modified index ellipsoid can be formulated as

$$\left(\frac{1}{n_o^2}+r_{13}E_z\right)x^2+\left(\frac{1}{n_o^2}+r_{23}E_z\right)y^2+\left(\frac{1}{n_e^2}+r_{33}E_z\right)z^2+2yzr_{42}E_y+2xzr_{51}E_x = 1. \tag{4.12}$$

Here, n_o and n_e represent the ordinary and extraordinary refractive indices, respectively. We consider the case where the a-, b-, and c-axis of the crystal are aligned with the x, y, and z coordinate axis, respectively (Fig. 4.8a). To determine the conditions for maximizing the index change, we need to perform a principal axis transformation. Our calculations follow the methodology outlined in Ref. [206], and show achievable index changes using the Pockels coefficients of bulk BTO.

***a*-axis oriented BTO**

We first consider the case of a-axis oriented BTO, where the x-axis of our coordinate system is oriented out-of-plane. For a resonator or waveguide structure on an a-axis oriented BTO film, an example of which is shown in Fig. 4.8b, we can identify two methods of optical excitation. In a TM mode (Fig. 4.8c), the primary direction of the optical electric field is out-of-plane (along the x-axis). In contrast, in a TE mode (Fig. 4.8d), the primary component of the optical electric field is in-plane, either along the y- or z-axis [206, 207]. In a waveguide structure such as the one shown in [206], the specific in-plane direction depends on the waveguide orientation, with the optical electric field being perpendicular to it.

We can now qualitatively determine which electro-optic coefficients primarily contribute to the index change using Eq. (4.12) and the orientation of the applied field:

1. **Applied external field along** E_z (waveguide oriented along y, Fig. 4.8e): For a TE mode, the optical electric field is primarily along the z-axis, leading to a dominant contribution from r_{33}. For a TM mode, the optical electric field is along the x-axis and modulation arises primarily from r_{13}.

2. **Applied external field along** E_y (waveguide oriented along z, Fig. 4.8f): Significant refractive index modulation simultaneously requires nonzero y- and z-components of the optical electric field. However, in a TE mode, the optical electric field is along the y-axis, while a field along the x-axis is obtained for a TM mode.

3. **Applied external field along** E_x: A similar argument as in the case of an applied field along E_y holds in this case. The condition of having an electric field simultaneously along the x- and z-axes cannot be satisfied.

While r_{33} can effectively create index modulation in one of the configurations discussed above, the highest Pockels coefficient, r_{42}, offers a pathway to more versatile modulators by relaxing certain design constraints. To utilize r_{42}, the resonator (or waveguide) needs to be oriented at an angle ϕ relative to the optical axis, as illustrated in Fig. 4.9a. This configuration allows us to introduce a rotated coordinate system (x', y', z') which is defined as

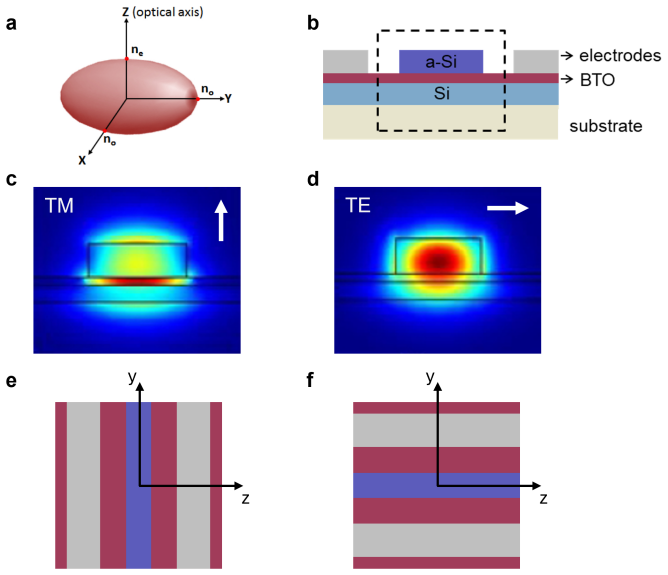

Figure 4.8: **BTO crystal orientation and resonator layout.** (a) Orientation of the index ellipsoid relative to coordinate system, with the optical axis (c-axis) aligned along z. The intersections of the index ellipsoid with the principal axes define the ordinary and extraordinary refractive indices, n_o and n_e, respectively. (b) Cross-section of waveguide structure studied in Ref. [206], featuring an a-axis oriented BTO thin film (magenta). Electric field profile of (c) TM and (d) TE modes, respectively. Arrow in the upper right indicates the orientation of the optical electric field within the BTO film. In-plane waveguide configurations are shown for (e) a waveguide along y (purple) with an applied field along z (between gray electrodes), and (f) a waveguide along z and applied field along y. Figures adapted from Ref. [206].

$$\begin{aligned} x &= x' \\ y &= y' \cos\phi + z' \sin\phi \\ z &= -y' \sin\phi + z' \cos\phi. \end{aligned} \tag{4.13}$$

When an external field $E_{z'}$ is applied, the field components transform as $E_y = E_{z'} \sin\phi$ and $E_z = E_{z'} \cos\phi$. We can then substitute these into Eq. (4.12) and analyze separately for TE and TM modes. For the TE mode, the optical electric field is nonzero only along the z'-axis ($x' = y' = 0$). This simplifies the expression to

$$\left[\frac{1}{n_o^2}\sin^2\phi + \frac{1}{n_e^2}\cos^2\phi + [(r_{13}+2r_{42})\cos\phi\sin^2\phi + r_{33}\cos^3\phi]E_{z'}\right]z'^2 = \left[\frac{1}{n_{z'}^2} + r_{z'}E_{z'}\right]z'^2 = 1. \tag{4.14}$$

Here, $n_{z'}$ and $r_{z'}$ are the effective refractive index and Pockels coefficients along the z'-direction, given by

$$\begin{aligned} n_{z'} &= \frac{n_o n_e}{\sqrt{n_e^2\sin^2\phi + n_o^2\cos\phi}} \\ r_{z'} &= r_{33}\cos^3\phi + (r_{13}+2r_{42})\cos\phi\sin^2\phi. \end{aligned} \tag{4.15}$$

Figure 4.9b illustrates the variation in $n_{z'}$ with ϕ for wavelengths between 400 to 700 nm. As the rotation angle increases from 0° to 90°, $n_{z'}$ transitions from n_e to n_o, reconnecting with the configurations discussed in Fig. 4.8e and f. The corresponding variation in $r_{z'}$ is shown in Fig. 4.9c, and reaches a maximum of $r_{z',\max} = 1025$ pm/V for $\phi = 54°$. In multi-domain BTO films, this optimal angle shifts closer to 45° [165, 193].

Finally, assuming $r_{z'}E_{z'} \ll n_{z'}^{-2}$, we can use the differential relation $dn = -\frac{1}{2}n^3 d\left(\frac{1}{n^2}\right)$ [146] to approximate the refractive index under an applied field, $n_{z',\text{field}}$, at the optimal angle as

$$n_{z',\text{field}} = n_{z'} - \frac{1}{2}n_{z'}^3 r_{z',\max}E_{z'}. \tag{4.16}$$

Figure 4.9d presents the effective index change, $|\Delta n_{z'}| = |n_{z'} - n_{z',\text{field}}|$, across the visible spectrum for an applied field of 0.1 MV/cm within BTO. For the calculations above, we use the refractive index values for BTO found in Ref. [208] and the unclamped Pockels coefficients summarized in Table 4.3.

We can repeat a similar analysis for the TM mode, where the optical electric field is only nonzero along the x'-axis and $y' = z' = 0$. Applying the principal axis transformation in this case results in the following equation

$$\left[\frac{1}{n_o^2} + r_{13}\cos\phi E_{z'}\right]x'^2 = \left[\frac{1}{n_{x'}^2} + r_{x'}E_{z'}\right]x'^2 = 1. \tag{4.17}$$

Here, the effective refractive index and Pockels coefficient along x', $n_{x'}$ and $r_{x'}$, are defined as

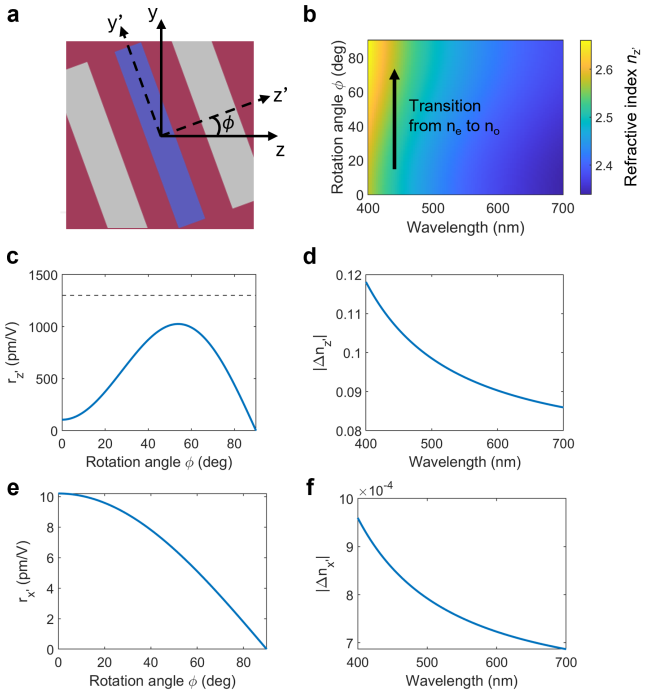

Figure 4.9: **Pockels coefficient and index change for a-axis BTO after principal axis transformation.** (a) In-plane rotation of principal axes by angle ϕ around the $x = x'$ rotation axis, resulting in new in-plane principal axes y' and z'. (b) Effective refractive index n'_z as function of rotation angle ϕ and wavelength. (c) Effective Pockels coefficient $r_{z'}$ for the TE mode as function of ϕ. The dashed gray line indicates the unclamped bulk value of r_{42} for reference. (d) Effective index change $|\Delta n_{z'}|$ as function of wavelength, calculated using the maximum $r_{z'}$ from (c) and an applied field of 0.1 MV/cm. (e) Effective Pockels coefficient $r_{x'}$ for the TM mode as function of ϕ. (f) Effective index modulation $|\Delta n_{x'}|$ as function of wavelength based on the maximal achievable value for $r_{x'}$ shown in (e) and an applied field of 0.1 MV/cm. All calculations assume a single-domain, a-axis oriented BTO film.

$$\begin{aligned} n_{x'} &= n_o \\ r_{x'} &= r_{13} \cos\phi. \end{aligned} \tag{4.18}$$

As shown in Fig. 4.9e, this configuration yields a significantly smaller Pockels coefficients with a maximum of $r_{x',\max} = r_{13} = 10.2$ pm/V at $\phi = 0$. This value is two orders of magnitude lower than the maximum effective Pockels coefficient, $r_{z',\max}$, discussed earlier. Consequently, the resulting refractive index change, $|\Delta n_{x'}|$, is also two orders of magnitude smaller, as depicted in Fig. 4.9f for the same applied field.

c-axis oriented BTO

In c-axis oriented BTO, the optical axis is aligned with the z-axis of the coordinate system, as shown in Fig. 4.8a. From Eq. (4.12), it is evident that leveraging r_{42} in this configuration requires an in-plane field (E_x, E_y, or a linear combination thereof). However, applying such fields to c-axis BTO films inevitably rotates the index ellipsoid, leading to a polarization rotation that complicates the design of pure phase or amplitude modulators.

The polarization rotation can be understood by considering a representative case of a field applied along the x-axis ($E_x \neq 0$) while $E_y = E_z = 0$. Under these conditions, equation (4.12) simplifies to

$$\frac{x^2}{n_x^2} + \frac{y^2}{n_y^2} + \frac{z^2}{n_z^2} + 2xzr_{42}E_x = 1. \tag{4.19}$$

The resulting principal axis transformation corresponds to a rotation around the y-axis by an angle θ, and is given by

$$\begin{aligned} x &= x' \cos\theta + z' \sin\theta \\ y &= y' \\ z &= -x' \sin\theta + z' \cos\theta. \end{aligned} \tag{4.20}$$

After this transformation, the index ellipsoid along the new principal axes (x', y', z') becomes

$$\left(\frac{1}{n_x^2} - r_{42}E_x \tan\theta\right)x'^2 + \frac{y'^2}{n_y^2} + \left(\frac{1}{n_z^2} + r_{42}E_x \tan\theta\right)z'^2 = \frac{x'^2}{n_{x'}^2} + \frac{y'^2}{n_{y'}^2} + \frac{z'^2}{n_{z'}^2} = 1. \tag{4.21}$$

Under the assumption that $r_{42}E_x \tan\theta \ll \frac{1}{n_x^2}$, we can write the effective refractive indices as

$$\begin{aligned} n_{x'} &= n_x + \frac{1}{2}n_x^3 r_{42}E_x \tan\theta \\ n_{y'} &= n_y \\ n_{z'} &= n_z - \frac{1}{2}n_z^3 r_{42}E_x \tan\theta \end{aligned} \tag{4.22}$$

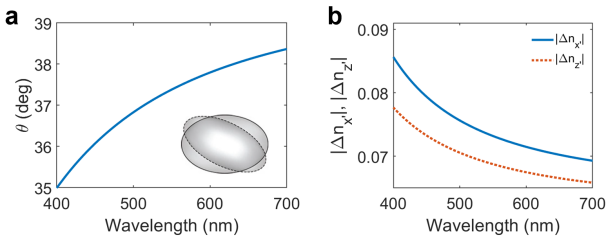

Figure 4.10: **Rotation of index ellipsoid and index change for c-axis BTO after principal axis transformation.** (a) Rotation angle θ as function of wavelength for an applied field of 0.1 MV/cm. The inset illustrates a schematic of an index ellipsoid rotated around the out-of-plane y-axis (dashed). (b) Effective refractive index modulation $|\Delta n_{x'}|$ (solid blue) and $|\Delta n_{z'}|$ (dotted orange) along the transformed principal axes (x', z') based on the rotation angle in (a) and an applied field of 0.1 MV/cm.

and the rotation angle is determined by

$$\tan 2\theta = -\frac{2r_{42}E_x}{\frac{1}{n_x^2} - \frac{1}{n_z^2}}. \tag{4.23}$$

Figure 4.10 shows the rotation angle θ and the change in effective refractive indices $|\Delta n_{x'}|$ and $|\Delta n_{z'}|$ as function of wavelength for an applied field of 0.1 MV/cm. Here, we used $n_x = n_o$ and $n_z = n_e$. While the achievable index changes in c-axis BTO are smaller than those attainable with a-axis BTO for a TE mode, they are comparable in magnitude and could enable the design of active polarization modulators (discussed further in Section 4.8).

4.5 Active transmissive metasurfaces: Unit cell design

BTO is an especially attractive material for active metasurfaces due to its superior electro-optic properties, short response times, high refractive index, and broad transparency window spanning visible to near-infrared wavelengths. These characteristics make it highly suitable for dynamic phase and amplitude modulation. This study focuses on active metasurfaces operating at red, green, and blue wavelengths (λ = 630, 532, and 460 nm, respectively), with a particular focus on transmissive designs. Unlike reflective metasurfaces, transmissive metasurfaces enable seamless integration with chip-scale light sources to create monolithic, ultra-compact optical devices capable of dynamic wavefront shaping. However, the shorter interaction length in transmissive metasurfaces typically necessitates more sophisticated designs with higher quality factors, making both their design and experimental

realization considerably more challenging. As a result, the majority of active metasurface research to date has focused on reflective devices.

Previous studies have shown that nanoblock resonators made from amorphous silicon (a-Si) can achieve active beam steering in transmission [80]. These resonators leverage higher-order Mie resonances to attain high quality factors [209], enabling precise wavefront manipulation. Building on these principles, nanoblock resonators composed of BTO can offer comparable functionality across multiple wavelengths while simultaneously achieving shorter response times. As detailed in Section 4.4, refractive index changes of approximately 0.1 or higher are achievable in a-axis BTO under applied fields of 0.1 MV/cm, with further increases possible at higher fields. This index modulation, combined with negligible optical losses and high-quality resonances, has the potential to support large phase modulation ranges potentially extending up to 2π.

Although BTO has a lower refractive index ($n_{\mathrm{BTO}} \sim 2.4 - 2.6$) compared to amorphous silicon ($n_{\mathrm{a\text{-}Si}} = 3.45$), comparable quality factors can be attained by increasing the nanoblock dimensions relative to the operation wavelength. These BTO resonators can be gated laterally using electrodes made from a variety of materials, including metals (Au, Ag, Cu, *etc.*), dielectrics (ITO, AZO, PEDOT, *etc.*), or doped BTO itself (*via* diffusion, implantation, thermal reduction, *etc.*). The lateral gating configuration ensures that the external electric field is parallel to the in-plane optical field, thereby leveraging the high r_{42} Pockels coefficient of BTO.

Active nanoantenna design using avoided crossing

Our transmissive metasurface design incorporates an array of BTO nanoblock resonators with lateral ITO electrodes, positioned on a SiO_2 dielectric spacer and a silicon nitride (Si_3N_4) membrane. The resonators are composed of a-axis BTO and oriented at the optimal angle of $\phi = 54°$ from the in-plane optical axis to maximize the effective Pockels coefficient, as illustrated in Fig. 4.9c. The effective refractive indices of BTO in this configuration are given by

$$
\begin{aligned}
n_x^T &= n_{z'} = \frac{n_o n_e}{\sqrt{n_e^2 \sin^2\phi + n_o^2 \cos^2\phi}} \\
n_y^T &= n_{y'} = \frac{n_o n_e}{\sqrt{n_e^2 \sin^2(\phi + \pi/2) + n_o^2 \cos^2(\phi + \pi/2)}} \\
n_z^T &= n_{x'} = n_o
\end{aligned}
\tag{4.24}
$$

where the notation x^T, y^T, and z^T is adopted for consistency with conventional coordinate systems. These axes correspond to the z', y', and x' axes, respectively (Fig. 4.9a).

Using a Si_3N_4 membrane as the underlying substrate reduces refractive index mismatch and minimizes optical mode perturbations in the BTO resonator. Furthermore, Si_3N_4 exhibits low optical losses at visible wavelengths [210], making it well-suited for operation at red, green, and blue wavelengths. We opt for a membrane thickness of 200 nm to balance optical compatibility with mechanical stability and robustness for future device fabrication. The reduced substrate thickness also facilitates the realization of ultra-thin functional optical elements that seamlessly integrate into advanced optical systems.

In transmissive metasurfaces, achieving a phase shift greater than π is often challenging due to shorter interaction lengths compared to reflective designs. One approach is to operate at points where two resonances merge, leveraging the combined phase shift at critical coupling. However, this often results in significant absorption, thus compromising absolute transmittance and efficiency. To overcome this limitation, we incorporate a thin SiO_2 spacer layer, which allows us to manipulate the coupling of modes. By optimizing the spacer thickness, we engineer an avoided crossing, which facilitates large and slowly varying phase shifts alongside high transmittance values [211], as detailed below.

Figure 4.11a shows the optimized layout of the metasurface unit cell for operation at red ($\lambda = 630 \pm 10$ nm). The nanoblock resonator has lateral dimensions of $w_x = 160$ nm, $w_y = 300$ nm, and a height of $h = 180$ nm. A larger width along the y^T axis was chosen due to a lower effective refractive index of BTO along that axis ($n_x^T = 2.69$, $n_y^T = 2.38$ at $\lambda = 630$ nm). The SiO_2 spacer thickness is $d = 40$ nm, and the membrane thickness is $t = 200$ nm. The BTO resonator is gated laterally in equipotential rows along the y^T axis for one-dimensional wavefront shaping. For the electrodes, we use ITO modeled as a Drude material with a carrier concentration

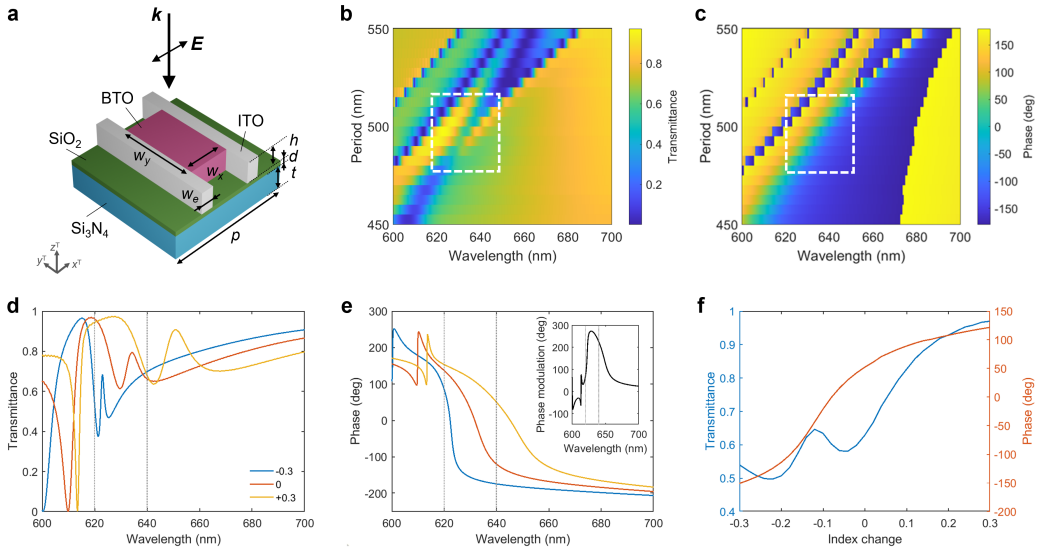

Figure 4.11: **Unit cell design of active transmissive metasurface based on BTO.** (a) The unit cell consists of an a-axis oriented BTO nanoblock resonator with dimensions $w_x = 160$ nm, $w_y = 300$ nm, and height $h = 180$ nm. The resonator is placed on top of a SiO_2 spacer layer of thickness $d = 40$ nm, and a Si_3N_4 membrane with thickness $t = 200$ nm. Lateral gating of the resonator is achieved with ITO electrodes having a width $w_e = 50$ nm and height $h = 180$ nm. The unit cell period is $p = 490$ nm, which is equal in both x^T and y^T direction. The metasurface is illuminated with a normally incident plane wave that is linearly polarized along the x^T direction. (b) Transmittance and (c) phase response as functions of period and wavelength. The white dashed boxes highlight an avoided crossing with high transmittance and large associated phase shift. (d) Transmittance and (e) phase response for a unit cell period of $p = 490$ nm, shown for three different values of refractive index change (Δn) in the BTO resonator along the x^T direction: $\Delta n = -0.3$ (blue), $\Delta n = 0$ (orange), $\Delta n = +0.3$ (yellow). The gray dotted lines in both plots indicate the target operation regime of $\lambda = 630 \pm 10$ nm. The inset in (e) shows the phase modulation resulting from a change in Δn from +0.3 to −0.3. (f) Transmittance (left, blue) and acquired phase (right, orange) as a function of refractive index change at a wavelength of $\lambda = 628.7$ nm, where the phase modulation is maximized.

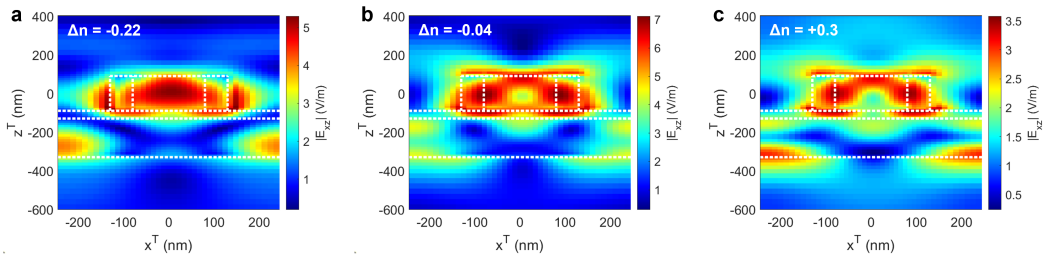

Figure 4.12: **Electric field distribution $|E_{xz}|$ in metasurface unit cell for varying index changes.** Magnitude of electric field in $x^T - z^T$ plane across the center of the BTO resonator for refractive index changes of (a) $\Delta n = -0.22$, (b) $\Delta n = -0.04$, and (c) $\Delta n = +0.3$ at $\lambda = 628.7$ nm.

of $N = 3 \cdot 10^{20}$ cm^{-3} and a mobility of $\mu = 40$ cm^2/(Vs). The ITO electrodes match the height of the BTO resonators to ensure a uniform field within the resonator.

All parameters, including the period p, were determined using a parameter sweep. As shown in Fig. 4.11b, an avoided crossing was identified at the target wavelength through a sweep of the period, as highlighted with the white dashed box. This region features high transmittance values that are simultaneously associated with a large, smoothly varying phase shift, as depicted in Fig. 4.11c. The maximal transmittance with large phase modulation is achieved for a period of $p = 490$ nm.

Based on a uniform index change in BTO along the x^T axis (applied field between the ITO electrodes), we simulated the transmittance and phase as functions of index change and wavelength. Figures 4.11d and e illustrate the transmittance and phase response for index changes of $\Delta n = -0.3$ (blue), 0 (orange), and +0.3 (yellow). The gray dashed lines denote the target operation window of $\lambda = 630 \pm 10$ nm. Our results show that transmittance above $\sim 37 - 68\%$ is maintained across these wavelengths, with higher minimum transmittance observed at redshifted wavelengths. The inset of Fig. 4.11e highlights the phase modulation attainable with an index change from $\Delta n = +0.3$ to -0.3, achieving a maximum phase modulation of 272.7° at a wavelength of $\lambda = 628.7$ nm. The associated transmittance modulation as a function of index change is shown in Fig. 4.11f, with the transmittance varying between $50 - 97\%$ at this wavelength.

Figure 4.12 depicts the electric field distribution across the center of the metasurface unit cell in the $x^T - z^T$ plane. We show the field profiles for the two transmittance dips in Fig. 4.11e at $\Delta n = -0.22$ (a) and $\Delta n = -0.04$ (b), which correspond to

distinct resonant modes. For $\Delta n = -0.22$, the mode is strongly confined within the resonator, whereas for $\Delta n = -0.04$, the electric field redistributes and shifts toward the edges of the resonator and the ITO electrodes. This redistribution highlights the need to investigate the sensitivity of the metasurface response to variations in ITO properties in future work. By contrast, for an index change of $\Delta n = +0.3$ (Fig. 4.12c), where we obtain highest transmittance, the electric field coupling to the resonator is significantly weaker. The weak coupling is evident from the low field strength and broader field distribution extending beyond the resonator, resulting in high transmittance. We note that in all three cases, a considerable portion of the electric field resides in the Si_3N_4 membrane. This behavior has implications for the design and implementation of beam steering metasurfaces, and will be further explored in Section 4.6.

Electrostatic simulations

The electromagnetic simulations described above are complemented by electrostatic simulations (Fig. 4.13), confirming that the desired index changes can be achieved with modest applied voltages. Specifically, we find that a refractive index change of 0.2 at $\lambda = 632$ nm is attainable with an applied voltage of 6 V across a BTO resonator with a width of $w_x = 180$ nm. Scaling these results to the unit cell design shown in Fig. 4.11a, an applied voltage of 8 V between the ITO electrodes will be sufficient to induce an index change of 0.3.

We note that this index change can only be achieved by patterning of lateral ITO electrodes that are directly adjacent to the BTO resonator and fully cover its sidewalls. Due to the high relative permittivity of BTO, there is a strong sensitivity of the refractive index change Δn to the presence of air gaps between the resonator and the ITO electrode. We characterize this air gap by the distance w_{air} between the resonator and the electrode. Our simulations indicate that an air gap as small as 5 nm will cause a nearly two-order-of-magnitude reduction in Δn (Fig. 4.13b).

These numerical findings are corroborated by analytical calculations, assuming a BTO relative permittivity of $\epsilon_{\text{BTO}} = \epsilon_x^T = 2400 \cdot \sin\phi + 60 \cdot \cos\phi$ with $\phi = 54°$, reflecting values in the clamped case. The electric field, E_x, is calculated as

$$E_x = \frac{\epsilon_{\text{air}} \cdot w_{\text{x,BTO}}}{\epsilon_{BTO} \cdot w_{\text{air}} + \epsilon_{air} \cdot w_{\text{x,BTO}}} \cdot \frac{V_{\text{applied}}}{w_{\text{x,BTO}}} \tag{4.25}$$

where $\epsilon_{\text{air}} = 1$, $w_{\text{x,BTO}}$ is the lateral dimension of the BTO resonator along the x^T direction, and V_{applied} is the applied voltage. The refractive index change within the

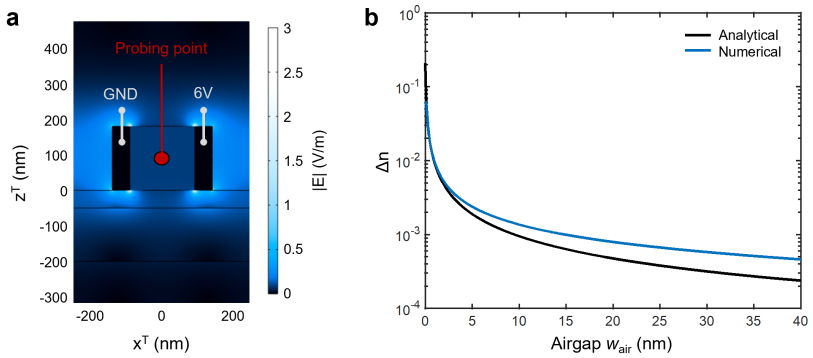

Figure 4.13: **Electrostatic simulations of BTO metasurface unit cell.** (a) Magnitude of electric field in $x^T - z^T$ plane across the center of the BTO resonator assuming an applied voltage of 6 V between the two ITO electrodes. The refractive index change Δn is probed at the center of the nanoblock, marked with the red spot. (b) Analytical (dark blue) and numerically obtained (light blue) refractive index change Δn as function of a distance, characterized by the width w_{air} introduced between the nanoblock and the ITO electrode on each side.

BTO resonator is then approximated using $\Delta n = 0.5 \cdot n_{\text{BTO}}^3 r_{\text{eff},54^\circ} E_x$ and is shown using the dark blue curve in Fig. 4.13b. Here, $r_{\text{eff},54^\circ} = 1025$ pm/V and $n_{\text{BTO}} = 2.45$ around $\lambda = 630$ nm.

To fabricate a BTO resonator with fully covered sidewalls forming ITO electrodes, two approaches are viable: angled sputtering to coat the sidewalls, or uniform ITO deposition over the entire metasurface followed by selective etching between the electrodes. Future work will focus on realizing designs with simplified fabrication processes, such as using lateral ITO electrodes with a shorter height, partially etching the BTO layer to replace the spacer layer with unetched BTO, or integrating the electro-optic BTO layer with higher-order Huygens metasurface structures composed of other low-loss dielectrics (such as silicon, amorphous silicon, gallium arsenide). Such designs could simultaneously benefit from high quality factors and the electro-optic tunability of BTO.

Angular dispersion

In addition to discussing the sensitivity of the observed mode to fabrication errors, it is essential to evaluate the system-level sensitivity. Specifically, this pertains to the incident angle of the illuminating plane wave, which can introduce perturbations to the optical mode and thereby affect the reported transmittance and phase modulation. Here, we examine the case where the metasurface is illuminated by a plane incident at

an angle θ relative to the z^T-axis within the $x^T - z^T$ plane, as illustrated in Fig. 4.14a. Our simulations of the transmitted intensity and phase reveal that features similar to those observed at the avoided crossing under normal incidence – characterized by high transmittance and a large, smoothly varying phase shift – can be observed up to an incident angle of approximately 2°, as indicated by the black dashed boxes in Fig. 4.14b and c, respectively. While these results demonstrate some tolerance to the incident angle, the stronger angular selectivity of this design compared to alternative metasurface designs [209], suggests the presence of a degree of nonlocality in the optical mode which contributes to achieving this performance.

An analysis of the transmittance and phase curves as function of refractive index changes indicates that as the incident angle increases from $\theta = 0°$ to 2° (Fig. 4.14d-f), additional higher-Q modes begin to emerge. At the wavelength corresponding to peak phase modulation at normal incidence ($\lambda = 628.7$ nm), a phase modulation of up to 251° is still maintained at $\theta = 2°$ (Fig. 4.14f). However, this is accompanied by a significant increase in transmittance modulation, evident from the appearance of additional modes with refractive index variation (blue and yellow curves). The heightened transmittance modulation will likely reduce performance in applications such as beam steering at these larger incident angles, as previously discussed in Section 2.4. Nonetheless, such metasurface designs may find greater utility in alternative applications, such as optical filters or angularly selective sensors, where strong angular sensitivity is advantageous.

4.6 Beam steering at red wavelengths

To demonstrate a specific application of the proposed BTO-based metasurface design, we analyze its beam steering efficiency in transmission and compare it to previously reported values for the reflective field-effect tunable plasmonic metasurfaces discussed earlier in this thesis [42, 46]. For this analysis, we consider the case of a normally incident plane wave, as shown in Fig. 4.11.

Since the proposed design incorporates lateral ITO electrodes that fully cover the sidewalls of the BTO resonator, we can assume an array configuration with spatially varying, periodic refractive index changes, where the index change is uniform throughout the BTO resonator, as schematically depicted in Fig. 4.15a-c. To simplify the analysis, we adopt a forward design approach, assuming equidistant index variations between adjacent metasurface unit cells within a supercell period. This configuration could be further refined by selecting index variations based on

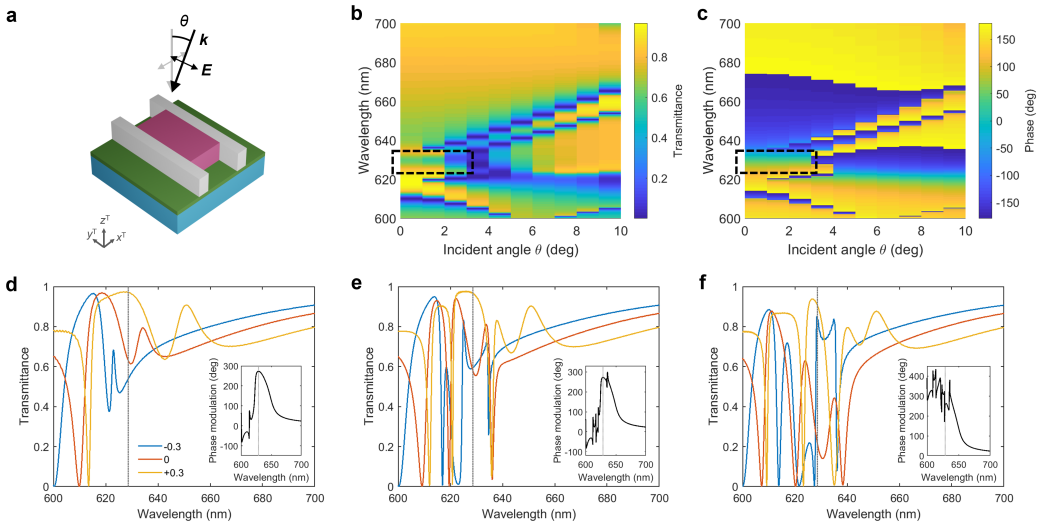

Figure 4.14: **Angular dispersion of resonant mode.** (a) Schematic illustration of metasurface unit cell illuminated by a plane wave incident at an angle θ relative to the surface normal (z^T-axis). The electric field E lies perpendicular to the incident wave vector $\boldsymbol{k}$ in the $x^T - z^T$ plane. (b) Transmittance and (c) phase as function of the incident angle θ and wavelength. The black dashed boxes mark regions displaying features similar to those observed at the avoided crossing under normal incidence (high transmittance and large, smoothly varying phase shift). (d)-(f) Transmittance as function of wavelength for refractive index changes of $\Delta n = -0.3$ (blue), $\Delta n = 0$ (orange), $\Delta n = +0.3$ (yellow) for incident angles of (d) $\theta = 0°$, (e) $\theta = 1°$, and (f) $\theta = 2°$. Insets in each panel show the associated phase modulation as a function of wavelength for refractive index changes from $\Delta n = -0.3$ to $+0.3$. The gray dotted line indicates the wavelength of peak phase modulation at normal incidence, located at $\lambda = 628.7$ nm.

equidistant phase modulation or, more effectively, through an array-level inverse design strategy that optimizes the index value at each unit cell to account for both phase and transmittance modulation [46].

As demonstrated by the mode profiles of the metasurface unit cell (Fig. 4.12) and its angular dispersion characteristics (Fig. 4.14), the design exhibits a degree of nonlocality. Consequently, array-level optimization in this case requires a numerical optimization approach. This process needs to be performed using numerical solvers, such as Lumerical FDTD, to accurately account for interantenna coupling effects and evaluate the true performance of the metasurface. Despite employing a simplified forward design methodology in this study, tunable diffraction is achieved with effective suppression of the specularly transmitted beam.

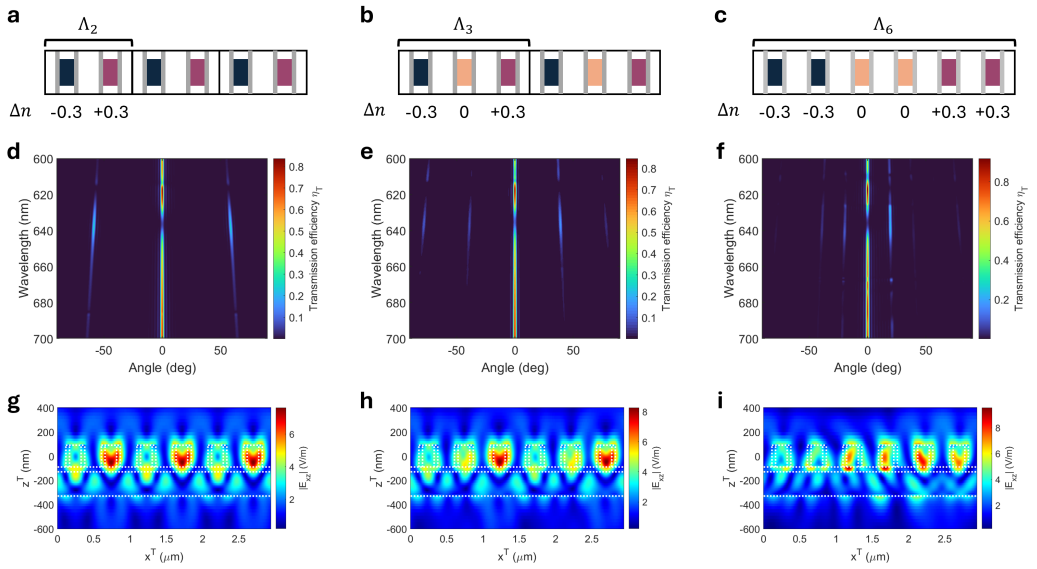

Figure 4.15: **Beam steering at red wavelengths in transmission.** (a-c) Top view schematic of metasurface array configuration for three different supercells consisting of (a) two unit cells (Λ_2), (b) three unit cells (Λ_3), and (c) six unit cells (Λ_6). The BTO resonators are modeled with uniform refractive index variations $\Delta n = -0.3$ (dark blue), $\Delta n = 0$ (light orange), and $\Delta n = +0.3$ (magenta). (d-f) Simulated transmission efficiency η_T as function of wavelength and angle for the corresponding configurations shown in (a-c). The total array sizes are (d) 50×50, (e) 51×51, and (f) 54×54 unit cells, respectively. (g-i) Magnitude of electric field $|E_{xz}|$ in $x^T - z^T$ plane across the center of the BTO resonator for the configurations in (a-c), shown at the wavelength corresponding to maximal suppression of the zeroth diffraction order, with (g) $\lambda_{\text{max}} = 636.4$ nm, (h) $\lambda_{\text{max}} = 635.3$ nm, and (i) $\lambda_{\text{max}} = 635.8$ nm, respectively.

Figure 4.15 illustrates the transmission efficiency as function of wavelength and angle for three different metasurface array configurations. These configurations consist of supercells with period Λ containing two unit cells (Fig. 4.15a, Λ_2), three unit cells (Fig. 4.15b, Λ_3), and six unit cells (Fig. 4.15c, Λ_6). While the first two configurations assign a distinct index variation to each unit cell, the third configuration (Λ_6) utilizes three index variation values, each repeated twice. Figures 4.15d-f show beam steering as a function of angle for the three different cases, assuming square metasurface arrays with 50×50, 51×51, and 54×54 elements, respectively. The transmission efficiency, η_T, of the diffracted orders was evaluated by normalizing the transmitted intensity with the far-field intensity at 0° without a metasurface. The results are summarized in Table 4.4.

Supercell	$\lambda_{\max}$ (nm)	θ_{+1} (°)	$\eta_{T,+1}$	$\eta_{T,0}$
Λ_2	636.4	58.4°	24.2%	6.5%
Λ_3	635.3	38.9°	17.0%	10.8%
Λ_6	635.8	19.4°	22.7%	3.9%

Table 4.4: **Transmission efficiency and angle of diffracted orders.** For each supercell configuration shown in Fig. 4.15, we report the wavelength with maximal suppression of the zeroth diffraction order, $\lambda_{\max}$, the angle of the first diffracted order, θ_{+1}, the transmission efficiency of the first order, $\eta_{T,+1}$, and the transmission efficiency of the zeroth order $\eta_{T,0}$.

The metasurface is capable of steering light to a maximal diffraction angle of $\theta = \pm 58.4°$ using a supercell period consisting of two unit cells (Λ_2). As summarized in Table 4.4, suppression of the zeroth-order specularly transmitted beam is achieved in all three cases, with the highest suppression ratio between the first and zeroth orders observed for Λ_6. This increased suppression ratio for Λ_6, particularly compared to Λ_3, can be attributed to the repeated configuration of index variations, which limits the effect of crosstalk between adjacent unit cells caused by abrupt changes. We additionally note that the peak suppression ratio in all cases occurs at wavelengths that are slightly redshifted from the wavelength of peak phase modulation ($\lambda = 628.7$ nm). This redshift is linked to a reduced transmittance modulation at these wavelengths, with minimal transmittance modulation observed at $\lambda = 638.4$ nm (Fig. 4.11d).

Despite achieving a phase modulation greater than 250°, we cannot obtain complete suppression of the specularly transmitted light due to the nonlocality of the optical modes. This effect is most apparent when comparing the electric field distributions for Λ_3 and Λ_6, shown in Figs. 4.15h and i, respectively. For Λ_3, the optical mode is most evidently distorted within the BTO resonator for $\Delta n = 0$, whereas for Λ_6, a distortion is observed within the Si_3N_4 membrane. Despite this crosstalk, we are able to successfully demonstrate tunable beam steering using conventional forward design methods. Notably, in comparison to previously realized plasmonic field-effect tunable metasurfaces [46], where the maximal efficiency of the diffracted order *after* an array-level inverse design approach was 2.7%, the current all-dielectric metasurface design achieves a nearly tenfold increase, with transmission efficiencies approaching 25% for Λ_2. Future enhancements in the transmission efficiency of the diffracted order could be realized through an optimization of the unit cell design with the objective to minimize crosstalk between adjacent elements or to reduce

transmittance modulation while maximizing phase modulation, as well as through system-level improvements leveraging array-level inverse design strategies.

4.7 Extension to RGB wavelengths

Electro-optically tunable metasurfaces based on barium titanate offer the distinct advantage of a broad transmission window that spans from the visible to the mid-infrared spectrum. This characteristic makes BTO particularly attractive for the realization of metasurfaces that operate at multiple wavelengths, relying on similar optical modes with slightly modified designs. In this section, we demonstrate a proof of concept for metasurface designs capable of operating at red, green, and blue (RGB) wavelengths, specifically $\lambda = 630 \pm 10$ nm, 532 ± 10 nm, and 460 ± 10 nm, respectively. To model the refractive index values of BTO across the visible spectrum, we use the dispersion relations provided by Wemple *et al.* [208]:

$$\begin{aligned} n_o^2 - 1 &= \frac{4.064\lambda^2}{\lambda^2 - 0.211^2} \\ n_e^2 - 1 &= \frac{4.187\lambda^2}{\lambda^2 - 0.223^2}. \end{aligned} \tag{4.26}$$

To facilitate future integration of RGB resonators in a single metasurface array, we designed all structures with consistent layer thicknesses. For this purpose, we first blueshift the design shown in 4.11 to enable operation at $\lambda = 532$ nm, and find comparable performance with nanoblock dimensions of $w_x = 120$ nm, $w_y = 250$ nm, and $h = 150$ nm, and a period of $p = 380$ nm. Building on this, we then extended the design to $\lambda = 630$ nm and $\lambda = 460$ nm. The optimized dimensions for all three designs are summarized in Table 4.5.

$\lambda_{\text{max phase}}$ (nm)	w_x (nm)	w_y (nm)	p (nm)
632.7	220	280	490
531	120	250	380
459.4	100	200	400

Table 4.5: **Dimensions for metasurface unit cell at red, green, and blue wavelengths.** The wavelength yielding maximal phase modulation $\lambda_{\text{max phase}}$ is reported together with the lateral resonator dimensions w_x and w_y, respectively, and the unit cell period p. All resonators are designed with a uniform height of $h = 150$ nm, a dielectric spacer thickness $d = 40$ nm, and a membrane thickness $t = 200$ nm.

Figures 4.16a-c illustrate the transmittance and phase modulation as function of index change for each resonator at the wavelength of maximal phase modulation,

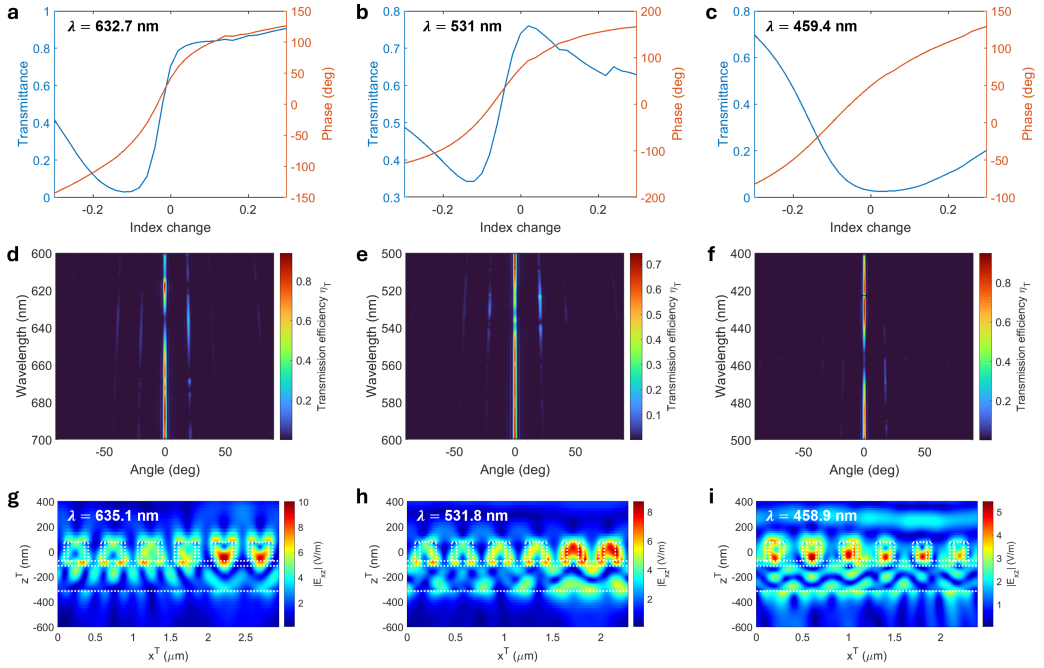

Figure 4.16: **Unit cell performance and beam steering at red, green, and blue wavelengths.** (a-c) Transmittance and phase modulation as function of a refractive index change from −0.3 to +0.3 shown at the wavelength of peak phase modulation (a) $\lambda_{\text{max phase}} = 632.7$ nm, (b) $\lambda_{\text{max phase}} = 531$ nm, and (c) $\lambda_{\text{max phase}} = 459.4$ nm. (d-f) Transmission efficiency η_T as function of wavelength and angle for the three resonator designs specified in Table 4.5. (g-i) Electric field distribution E_{xz} across the center of the BTO resonator in the $x^T - z^T$ plane at the wavelength of maximal suppression of the zeroth transmitted order.

$\lambda_{\text{max phase}}$. The average transmittance is highest for the green-wavelength resonator, as this design was specifically optimized for its performance, whereas the red and blue designs were subject to additional constraints to maintain a consistent resonator height. For the red wavelength (Fig. 4.16a), the average transmittance is 54%, accompanied by a phase modulation of 269° at $\lambda = 632.7$ nm. At the green wavelength (Fig. 4.16b), we achieve an average transmittance of 56% with a phase modulation of 293° at $\lambda = 531$ nm. Finally, for operation at the blue wavelength (Fig. 4.16c), an average transmittance of 21% is achieved together with a phase modulation of 212°. These variations in transmittance and phase modulation can be attributed to different optical modes given a fixed height across all three designs, as well as differences in the refractive index at the respective wavelengths. We note that all three resonators were analyzed under an index modulation of $\Delta n = \pm 0.3$ which

corresponds to different applied voltages for each case. Based on the resonator width w_x specified in Table 4.5, the required applied voltages are 11 V, 6 V, and 5 V for red, green, and blue, respectively.

Next, we analyzed the beam steering performance by evaluating the transmission efficiency η_T as function of wavelength and angle for each design. For all three designs, we consider the configuration schematically depicted in Fig. 4.15c with the supercell Λ_6, consisting of two repetitions of three equidistant refractive index variations. The transmission efficiency results for the diffracted order and zeroth order are summarized in Table 4.6.

$\lambda_{\max}$ (nm)	θ_{+1} (°)	$\eta_{T,+1}$	$\eta_{T,0}$
635.3	19.4°	24.0%	5.1%
531.8	21.0°	12.4%	18.9%
458.9	17.2°	7.2%	5.3%

Table 4.6: **Transmission efficiency and angle of diffracted orders for red, green, and blue wavelengths.** Reported are the wavelength of maximal suppression of the zeroth diffraction order, $\lambda_{\max}$, the angle of the first diffracted order, θ_{+1}, the transmission efficiency of the first order, $\eta_{T,+1}$, and the transmission efficiency of the zeroth order $\eta_{T,0}$.

Interestingly, the green-wavelength design achieves maximal phase modulation with minimal transmittance modulation across these designs, however, it exhibits limited suppression of the zeroth order in the analyzed beam steering configuration. This limitation likely arises from its small unit cell period (p = 380 nm), resulting in increased coupling between adjacent resonators, as shown by the electric field distributions in Fig. 4.16h. Similarly, the blue-wavelength design shows hybridization of modes (Fig. 4.6i), however, a stronger zeroth-order suppression can be achieved in this case. In contrast, the red-wavelength design shows the least mode coupling (Fig. 4.6i), resulting in improved diffraction efficiency.

Further studies of the optical modes are required to fully understand these differences and optimize designs for higher suppression ratios between the first diffracted and zeroth orders. Despite these challenges, this study successfully demonstrates the feasibility of developing metasurfaces capable of operating at RGB wavelengths. Our findings provide a strong foundation for future optimization efforts aimed at integrating of these resonators into an RGB modulator array.

4.8 Outlook

In this chapter, we introduced a new synthesis method alongside designs for achieving high-efficiency transmissive metasurfaces for beam steering at visible wavelengths. While significant progress was made, several challenges remain for the experimental realization of these metasurfaces and their integration into practical applications. In the following, we outline key tasks that can build upon the insights gained in this work.

Spalling large-area single-domain BTO films

A critical requirement for integrating spalled BTO films in active metasurfaces is the production of large-area films that are both single-crystal and single-domain. Such films maximize the electro-optic response, enabling their use in diverse photonic applications. Our earlier studies demonstrated that the thickness of spalled films can be controlled through the thickness of electroplated Ni, which also influences the RMS roughness of the films. Specifically, we noted that thinner films exhibited smoother surfaces and likely experienced reduced domain switching caused by mechanical forces.

Extending this process to larger areas requires a deeper understanding of how mechanical stresses affect both roughness and thickness. Key questions include whether domain switching occurs as a static effect during electroplating or a dynamic process during spalling. Automating the spalling process rather than relying on manual exfoliation could ensure greater consistency and control, facilitating the fabrication of large spalled areas suitable for device integration.

Integration into RGB array

Optimizing individual metasurface resonators for distinct wavelengths (red, green, and bue) is the first step toward integrating them into a modulating element capable of multi-wavelength operation. Achieving this goal requires careful consideration of the resonator arrangement to maximize color accuracy and contrast while minimizing interelement crosstalk.

Configurations such as fully interdigitated arrays, such as the one shown in Fig. 4.17, may provide a solution for large fields of view. However, segmenting the array into subarrays of RGB pixels could reduce crosstalk and improve the color contrast [212]. Alternatively, stacking transmissive metasurfaces for each wavelength could facilitate multi-wavelength control. This approach, though promising, requires detailed analysis of losses introduced by non-resonant layers. Interestingly, stacked

configurations could also enable two-dimensional wavefront shaping by rotating each layer in-plane by 90°.

For arbitrary wavefront shaping, a two-dimensional interconnect scheme may be necessary. This would likely involve redesigning resonators, possibly with different crystal orientations, to allow for electric gating along both dimensions. While this approach could simplify wavefront shaping, it introduces additional design and fabrication complexities

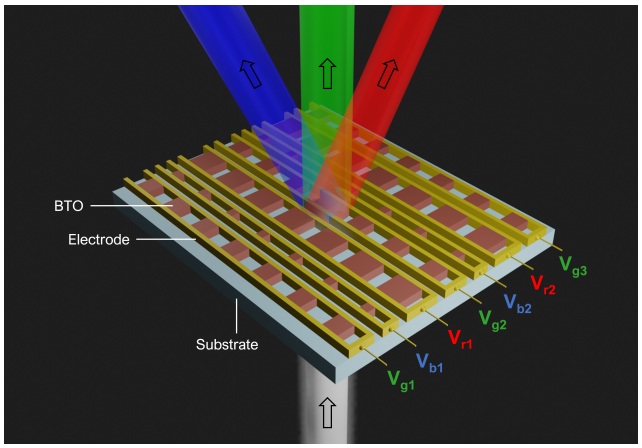

Figure 4.17: **BTO-based RGB modulator array.** Broadband (white) light is incident on an active transmissive metasurface consisting of resonators designed for RGB control. By applying individual gate voltages to each resonator n, $V_{\{r,g,b\},n}$, the transmitted beams can be split in distinct wavelengths and perform different operations at distinct wavelengths.

Fabrication and alternative design strategies

The experimental realization of transmissive metasurfaces based on the proposed designs requires precise fabrication of BTO nanoblock resonators with vertical sidewalls. If BTO exhibits etching behavior similar to titanium dioxide (TiO_2), such precision may be feasible [213]. However, if its etch characteristics align more closely with other electro-optic materials such as lithium niobate, which typically etches with a sidewall angle [214], further studies will be needed to evaluate the impact of sidewall angles on optical performance.

An alternative approach for resonator design could involve relaxing etching requirements by including an underetched BTO layer to partially or fully replace the dielectric spacer. Alternatively, etching could be avoided entirely by using high-index materials such as Si or gallium arsenide (GaAs) for the resonators, while leveraging the electro-optic tunability of an underlying unetched BTO layer.

Additionally, adopting an out-of-plane electrode configuration instead of lateral gating may help mitigate crosstalk between metasurface elements by increasing the spacing between resonators. Such designs would likely benefit from c-axis BTO thin films, leveraging the r_{33} electro-optic coefficient. Although r_{33} is ten times smaller than r_{42} in BTO, it is three times higher than r_{33} in LN and may therefore relax the requirements for the resonator quality factor in comparison to LN.

Polarization tunability

In Section 4.4, we discussed the contributions from the electro-optic coefficients for various electrode configurations in a- and c-axis thin films. In c-axis BTO, applying an in-plane electric field rotates the index ellipsoid. In this case, when the incident wave vector is misaligned with the principal axes, the polarization state becomes a linear combination of normal modes dictated by the transformed index ellipsoid.

This electrically controllable rotation of the index ellipsoid, as defined in equation (4.23), could be exploited for realizing polarization-tunable elements. However, achieving this requires a comprehensive understanding of the BTO anisotropy, resonator optical modes, and the interplay between the electro-optic effect, crystal orientation, and applied electric field. Advanced numerical modeling and experimental validation will be crucial for realizing these devices.

Realization of high-frequency modulators

The instantaneous electro-optic response of BTO makes it an ideal candidate for high-frequency modulators capable of spatiotemporal light manipulation. Previous studies have demonstrated modulation frequencies in the GHz range for BTO-based devices [193]. Developing such active metasurfaces will require optimizing resonator geometry, electrical addressing schemes, and overall interconnect layouts to minimize RC time constants. By incorporating these capabilities, metasurfaces could achieve precise control not only over amplitude, phase, polarization, and wavevector, but also frequency of light.

4.9 Conclusions

In summary, we have developed a scalable and cost-effective method for fabricating high-quality single-crystal BTO thin films suitable for integration in advanced functional devices. Spalled films can be obtained with desired crystal orientations, as demonstrated for (100) and (001) bulk crystals, with film thicknesses ranging from 100 nm to 15 μm and lateral dimensions spanning several hundred micrometers to

millimeters. The film thickness is controlled by the electroplated Ni layer, which dictates the stress state of the underlying BTO substrate. While stress-induced domain switching during spalling introduces surface roughness, the intrinsic properties of bulk BTO are preserved. We characterized the electro-optic Pockels coefficient of spalled BTO films after transfer to a rigid substrate and measured an electro-optic coefficient of $r_{33} = 55 \pm 5$ pm/V in multi-domain regions and $r_{33} = 160 \pm 40$ pm/V in smaller, likely single-domain regions. Our results indicate that spalled BTO films can exceed the performance of commercially available thin-film lithium niobate. Future work should focus on improving surface quality, controlling domain structures, and developing techniques for transferring isolated BTO thin membranes, broadening their applicability in scalable photonic device integration.

From a design perspective, we explored how BTO thin films that retain bulk electro-optic properties can be integrated into transmissive active metasurfaces. Using *a*-axis oriented films allows for a maximization of the effective electro-optic coefficient, which can be harnessed in resonant active metasurfaces. By applying an in-plane electric field at 54° to the optical axis, and using an incident plane wave polarized parallel to this field, an effective electro-optic coefficient of $r_{\text{eff}} = 1025$ pm/V can be achieved. This enables index changes of up to 0.3 at visible wavelengths with applied fields around 0.3 MV/cm. Such fields can be induced in BTO nanoblock resonators through lateral gating along the resonator sidewalls. Through careful engineering of the resonator geometry and underlying layers, we demonstrated an avoided crossing of optical modes, enabling high transmittance alongside a large, smoothly varying phase shift. Specifically, our transmissive metasurface design achieved a phase modulation of 272.7° with transmittance varying from 50-97% at $\lambda = 628.7$ nm assuming an index change of ±0.3. This design was also shown to enable active beam steering up to ±58°, with partial suppression of the zeroth-order transmitted beam due to resonator crosstalk. Using conventional forward design methods, we obtained a transmission efficiency of the diffracted beam ranges of around $17 - 24\%$, with further improvements anticipated through array-level inverse design approaches. Additionally, leveraging the broad transparency window of BTO, we showed that similar designs can be adapted for active beam steering at RGB wavelengths.

While significant efforts remain for the experimental realization of BTO-based transmissive metasurfaces, the advances outlined here establish a strong foundation for next-generation metasurfaces capable of comprehensive light control across multi-

ple dimensions. These developments mark a critical step toward active metasurfaces for universal light manipulation, paving the way for transformative applications in optical communication, computation, and imaging.